A comparative assessment of the vertical distribution of forest components using full-waveform airborne, discrete airborne and discrete terrestrial laser scanning data

Crespo-Peremarch, Pablo [1,*], Fournier, Richard A. [2], Nguyen, Van-Tho [2], van Lier, Olivier R. [3] and Ruiz, Luis Ángel [1]

[1] Geo-Environmental Cartography and Remote Sensing Group (CGAT), Department of Cartographic Engineering, Geodesy and Photogrammetry, Universitat Politècnica de València, Camí de Vera s/n, 46022, València, Spain.

[2] Department of Applied Geomatics, Centre d'applications et de recherché en télédétection, Université de Sherbrooke, 2500 boul. de l'université, J1K 2R1, Sherbrooke, QC, Canada.

[3] Natural Resources Canada, Canadian Forest Service – Canadian Wood Fibre Centre, A2H 5G4, NL, Canada.

Keywords: lidar, understory vegetation, occlusion, boreal forest, Mediterranean forest, Gini index.

[*] Corresponding author
Email address: pabcrepe@cgf.upv.es

Abbreviations in the manuscript
ALS (airborne laser scanning); TLS (terrestrial laser scanning); ALS_{FW} (full-waveform ALS); ALS_D (discrete ALS); Nh (number of hits); Nh^{ALS} (number of hits from ALS) Nh^{ALSFW} (number of hits from ALS_{FW}); Nh^{ALSD} (number of hits from ALS_D); Nt (number of theoretical laser beams passing through a voxel); Nb (number of theoretical beams that were occluded prior to reaching a voxel); PAD (plant area density); PAD^{TLS} (plant area density for TLS); NF (Newfoundland); SP (Spain).

Abstract

Laser scanning has the potential to accurately detect the vertical distribution of forest vegetative components. However, limitations are present and vary according to the system's platform (i.e., terrestrial or airborne) and recording method (i.e., discrete return or full waveform). Terrestrial configurations detect close objects (i.e., lower vegetation strata) in more detail while airborne configurations detect a more detailed upper strata, with weak backscattered signals from lower strata. Moreover, discrete lidar systems record single or multiple hits from a given pulse at intercepted features in contrast to full-waveform systems, which register the pulse's complete backscattered signal providing complete vertical profiles. In this study, we examine for a Boreal and a Mediterranean forest with contrasted conifer canopy densities: (*i*) the characterization of the vertical distribution and signal occlusion from three laser scanning configurations: full-waveform airborne (ALS_{FW}), discrete airborne (ALS_{D}), and discrete terrestrial (TLS); (*ii*) the comparison in the detection of understory vegetation by ALS_{FW} and ALS_{D} using TLS as reference; and (*iii*) the use of a methodological procedure based on the Gini index concept to group understory vegetation in density classes from both ALS_{FW} and ALS_{D} configurations. Our results demonstrate, firstly, that signal occlusion can be quantified by the rate of pulse reduction independently for data from all three laser scanning configurations. The ALS_{D} configuration was the most affected by signal occlusion, leading to weak signal returns at the lower strata ($z < 4$ m) where the rate of pulse reduction was highest as a result of dense canopy covers. Secondly, we demonstrated the capabilities for both airborne laser scanning configurations to detect understory vegetation, albeit significantly more accurately with ALS_{FW}. Lastly, we demonstrated the use of the Gini index as an indicator to determine understory vegetation density classes, particularly for ALS_{FW} data in dense canopy cover. We proceed to explain the limitations in detecting the

vertical distribution from different configurations, and indicate that understory vegetation density classes may be successfully assigned with ALS_{FW} in contrasted conifer canopy densities.

1. Introduction

Signal occlusion is the main limitation in acquiring fully comprehensive laser scanning datasets in forested environments. Signal occlusion occurs when the object to sample is partially or completely obscured by an intervening object. The presence and amount of signal occlusion found in a laser scanning dataset depends greatly on the scanning configuration (i.e., above-canopy for aerial or near-ground for terrestrial), vegetation cover and density, and its complexity (Watt and Donoghue, 2005). Signal occlusion can therefore limit the detection of a forest's horizontal and vertical distribution of vegetation, particularly in dense forested environments. It is important to note that signal occlusion is not to be confounded with forest cover. While forest cover refers to the proportion of forest covered by the vertical projection of tree crowns, signal occlusion refers to the shadow (lack of laser signal) caused by canopy elements. Several strategies have been tested to reduce signal occlusion such as increasing the number of flyovers for airborne laser scanning (ALS) (Kükenbrink et al., 2017), combining data from multiple sensors (Giannetti et al., 2018), or sampling the plot with multiple scans from varying viewpoints with a terrestrial laser scanning (TLS) (Martin-Ducup et al., 2017). Another way to deal with signal occlusion in TLS data is to divide the point cloud space into voxels and compute the Plant Area Density (PAD) for each voxel (Béland et al., 2014; Pimont et al., 2018). Analyzing signal occlusion and its effects on the estimation of forest structural attributes is essential in understanding the limitations of different laser scanning and sampling configurations, and therefore sampling designs to best minimize signal occlusion.

Although signal occlusion is present in all laser scanning datasets, ALS and TLS systems have nonetheless demonstrated their capability to characterize forest attributes with great precision

and accuracy. Among ALS sensors, traditional or discrete ALS (ALS_D) is now used operationally to estimate stand attributes for a wide range of forest ecosystems (Kankare et al., 2013a; Hevia et al., 2016; Bottalico et al., 2017), and to classify tree species and forest canopy fuels (Vaughn et al., 2012; Ruiz et al., 2018; Torralba et al., 2018). On the other hand, less attention has been attributed to full-waveform ALS (ALS_{FW}) sensors due to the data's greater complexity and the current lack of processing tools (Crespo-Peremarch et al., 2018a). ALS_{FW} data provides the complete signal emitted by the sensor as opposed to discrete hits. The data is processed as a continuous return signal providing information within the forest vertical components. Some studies have demonstrated the success of ALS_{FW} to estimate forest stand variables (Cao et al., 2014a; Cao et al., 2014b; Hermosilla et al., 2014a; Crespo-Peremarch et al., 2016) and classify tree species (Heinzel and Koch, 2011; Cao et al., 2016; Torralba et al., 2018). In comparison with ALS data, TLS data can provide a more detailed point cloud of a forest structure, albeit from a different viewpoint. For applications in forested environments, the useful portion of the TLS point cloud extent is often limited (10 – 30 m) with a hemispherical view around the sensor. Withstanding that, many studies have demonstrated the capabilities of TLS to estimate and extract forest stand variables (Srinivasan et al., 2015; Liang et al., 2016; Ravaglia et al., 2019), and fewer on the classification of tree species (Lin and Herold, 2016; Torralba et al., 2018).

Since ALS and TLS sensors acquire data from differing positions relative to the forests canopy, different occluded forest strata can be observed in their point clouds. Consequently, it is of interest to compare their independent effectiveness to detect the forests horizontal and vertical distribution, and estimate forest structural attributes. Several studies provide a base for

comparison between three laser scanning configurations: ALS_D, ALS_{FW} and TLS. These studies generally show that canopy height estimations are more accurate using ALS than TLS (Hilker et al., 2012; Crespo-Peremarch and Ruiz, 2017), while characterization of the foliage profile is estimated with more accuracy by TLS, especially in the lower strata (Chasmer et al., 2006; Hilker et al., 2010), where understory vegetation is found. On the other hand, other studies concur on a more accurate estimation of forest structural attributes from ALS_{FW} than ALS_D for canopy height (Anderson et al., 2016), aboveground biomass (Nie et al., 2017), stand volume (Lindberg et al., 2012), and the classification of species composition (Torralba et al., 2018).

A common challenge in predicting forest structure from ALS data is finding associated reference data from which reliable error estimation is possible. Most studies on forest structure variables use a combination of field measurements and allometric relationships as reference data (González-Ferreiro et al., 2012; Treitz et al., 2012; Ruiz et al., 2014). However, in cases where 3D assessments of vegetative material are required, it can be beneficial to use TLS data as a reference as these can be difficult and often logistically challenging to quantify directly from field activities. TLS data often represent the best available information to describe forest elements (Martin-Ducup et al., 2016; Crespo-Peremarch et al., 2018b; Ravaglia et al., 2019), being sampled in much more detail when compared with ALS. However, there are important discrepancies between ALS and TLS point clouds that need to be acknowledged. Looking at a vertical profile of data points in relative terms, ALS_D point clouds have far more hits within the upper canopy and on the ground, while most of the hits for TLS point clouds are located at the lower crown, trunks-stems, understory, and ground (Crespo-Peremarch and Ruiz, 2017). These differences in sampling capabilities lead to estimation divergences (Chasmer et al., 2006). In

general, ALS_D point clouds tend to under-represent the lower strata. While correlation between ALS_D and TLS point clouds has been found to be 0.48 for heights below 20 m, it reached 0.87 when only the upper canopy (z > 20 m) was considered (Hilker et al., 2010). As for canopy height, estimation from ALS_D and TLS were generally similar: (*i*) an underestimation of 1 m by the TLS in a mixed forest in Ontario, Canada (Chasmer et al., 2006), (*ii*) a correlation of 0.94 between estimations from both datasets in a pine-dominated forest in South-Korea (Jung et al., 2011), and (*iii*) a correlation near 1 in a coniferous forest on Vancouver Island, BC, Canada (Hilker et al., 2010). Conversely, other studies found ALS_D more suited to estimate canopy height than TLS: (*i*) with an R^2 of 0.96 and 0.86, respectively in a lodgepole pine forest in Alberta, Canada (Hilker et al., 2012), and (*ii*) with an underestimation of 2.1 m by the TLS in a Mediterranean forest (Crespo-Peremarch and Ruiz, 2017). Therefore, there are situations where ALS and TLS may not accurately estimate the entire vertical forest structure, primarily due to signal occlusion. This signal occlusion problem is more severe for ALS than it is for the TLS because of the much smaller number of laser pulses. Fortunately, the beam width and the multiple return configuration mitigate this problem. Consequently, sampling understory vegetation is comparably far more comprehensive from TLS than it is from ALS. TLS data are therefore suitable reference data for the estimation of understory structural attributes and preferred over using traditional field sampling techniques, which can be laborious and time consuming (Crespo-Peremarch et al., 2018b).

Within the vertical distribution of the forest, detection of the lower strata can be challenging from ALS sensors, especially from ALS_D as a result of signal occlusion from the overstory (Anderson et al., 2016; Crespo-Peremarch and Ruiz, 2017). Nonetheless, ALS_D has proven to

discriminate presence and absence of understory vegetation with promising accuracy (e.g., R^{2}`s of 0.83 (Martinuzzi et al., 2009), 0.77 (Hill and Broughton, 2009), 0.74 (Wing et al., 2012), and 0.48 (Morsdorf et al., 2010)) and has been demonstrated to be more accurately estimated by ALSFW than ALSD (Hancock et al., 2017; Torralba et al., 2018). In contrast, point clouds from TLS provide a large amount of detail on understory vegetation due to the position of the sensor (Liu et al., 2017). However, most studies have focused on the ability of TLS to characterize shrubs in ecosystems absent of overstory (e.g., Vierling et al., 2013; Olsoy et al., 2014; Greaves et al., 2015); few have focused on characterizing the understory vegetation from forested ecosystems (e.g., Chen et al., 2016). Furthermore, studies have estimated understory cover with ALS_{FW} using TLS as reference data and obtained a normalized root-mean-square error of 24% (Hancock et al., 2017) and 9% (Crespo-Peremarch et al., 2018b). Nevertheless, a limited amount of studies have compared the ability to estimate understory vegetation presence or distribution from these three different laser scanning datasets (i.e., ALS_{FW}, ALS_{D} and TLS) (e.g., Hancock et al., 2017; Torralba et al., 2018). These studies confirmed that ALS_{FW} and TLS are both capable of estimating the spatial distribution of understory vegetation in more detail than using ALS_{D} data, e.g., with overall accuracies of 86.4% and 77.3%, respectively (Torralba et al., 2018). These results demonstrate the potential of combining ALS_{FW} and TLS data in a workflow that estimates the spatial distribution of the understory vegetation beyond what can be estimated from ALS_{D} data. However, these results were limited in their application as they were assessed in a fragmented urban forest and an open Mediterranean forest.

The overarching goal of this study was to assess the ability of different laser scanning configurations to estimate vertical forest structure in natural forest environments. Specifically,

157 we investigated the independent capability of ALS_D, ALS_{FW} and TLS to estimate the amount and
158 spatial distribution of understory vegetation from the lower strata ($z < 4$ m) for two structurally
159 contrasting conifer dominated forests: a dense Boreal forest and an open Mediterranean forest.
160 Three specific objectives were defined to reach the overarching goal: (*i*) characterize the vertical
161 distribution and signal occlusion caused by vegetation in these two ecosystems from each
162 scanning configuration; (*ii*) determine whether ALS_{FW} allows detecting the distribution of
163 understory vegetation to a level of detail beyond ALS_D capability; and (*iii*) adapt a
164 methodological procedure to determine understory vegetation density from ALS_{FW} and ALS_D
165 point clouds.

166 # 2. Material and methods

167 ## 2.1. Study areas

168 Two study areas were selected based on their contrasting canopy densities and understory
169 vegetation presence. Both sites are conifer dominated, albeit, structurally very different. Our first
170 study area (111,257 ha) is located in a Boreal Shield Ecozone in western Newfoundland and
171 Labrador, Canada and centered around 49.04°N and 57.93°W (Fig. 1a). The ecoregion is
172 dominated (~70%) by forest land and is located within the most eastern boreal forest region of
173 North America. Balsam fir (*Abies balsamea* (L.) Mill)) is the dominant tree species of the region
174 followed by Black spruce (*Picea mariana* (Mill.) Britton, Sterns & Poggenb.). White birch
175 (*Betula papyrifera* Marsh.), yellow birch (*Betula alleghaniensis* Britton), white spruce (*Picea*
176 *glauca* (Moench) Voss) and eastern larch (*Larix laricina* (Du Roi) K. Koch) are present to a
177 much lesser extent. The relief is gently undulating to hilly with elevation ranges between ~30 m
178 and 640 m. Forest understory is extremely variable depending on stand density and age, soil
179 conditions, status of regeneration and silvicultural treatments such as precommercial thinning

(e.g., Fig. 2 – Newfoundland, sparse understory). Understory vegetation can be composed of tree saplings and seedlings, ferns (e.g., *Dryopteris carthusiana* (Vill.) HP Fuchs) and to a lesser extent ericaceous shrubs (e.g., *Kalmia angustifolia* L., *Rhododendron groenlandicum* (Oeder) Kron & Judd, *Vaccinium* spp.).

The second study area (3,742 ha) is located in a Mediterranean forest located in the Natural Park of Sierra de Espadán, in the eastern Spanish province of Castellón centered around 39.96°N and 0.41°W (Fig. 1b). The study area is dominated by Aleppo pine (*Pinus halepensis* Mill.), maritime pine (*Pinus pinaster* Ait.) and cork oak (*Quercus suber* L.). This province is the most mountainous in Spain with altitudes ranging from sea level to 1,813 m. The presence of understory in the study area is very variable, mainly depending on the dominant species and soil properties. Understory vegetation is dominated by the following shrubs and flowering plants: rosemary (*Rosmarinus officinalis* L.), tree heath (*Erica arborea* L.), brezo (*Erica multiflora* L.), Mediterranean buckthorn (*Rhamnus alaternus* L.), kermes oak (*Quercus coccifera* L.) and mastic (*Pistacia lentiscus* L.). Fig. 2 illustrates examples of different understory scenarios.

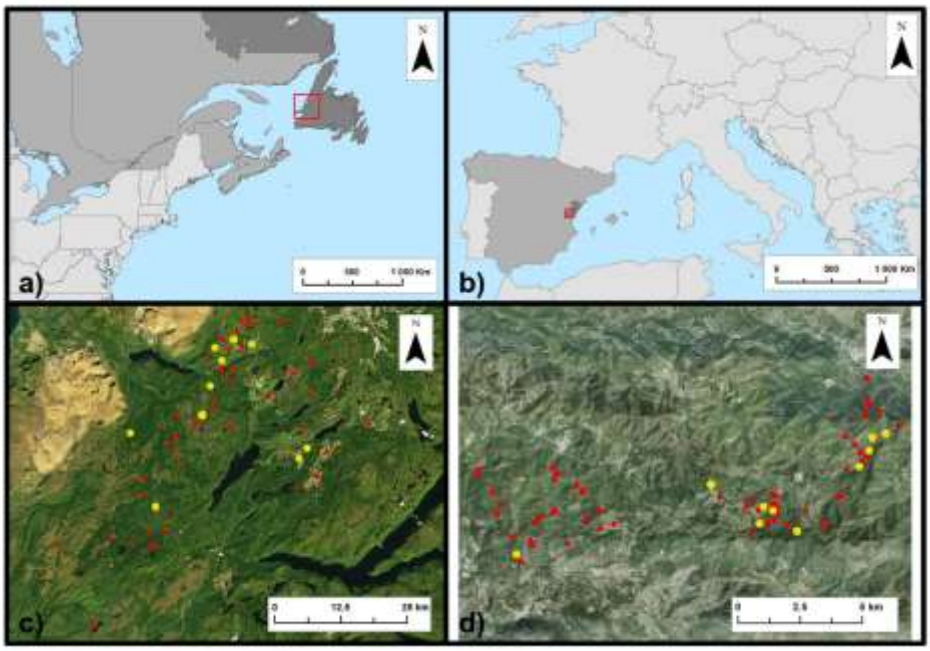

Fig. 1. Location of plots registered (red) and plots used in the current study (yellow) within each study area: (a, c) in western Newfoundland, Canada, and (b, d) in the Castellón province, Spain (Background imagery: PNOA andWorldView-2).

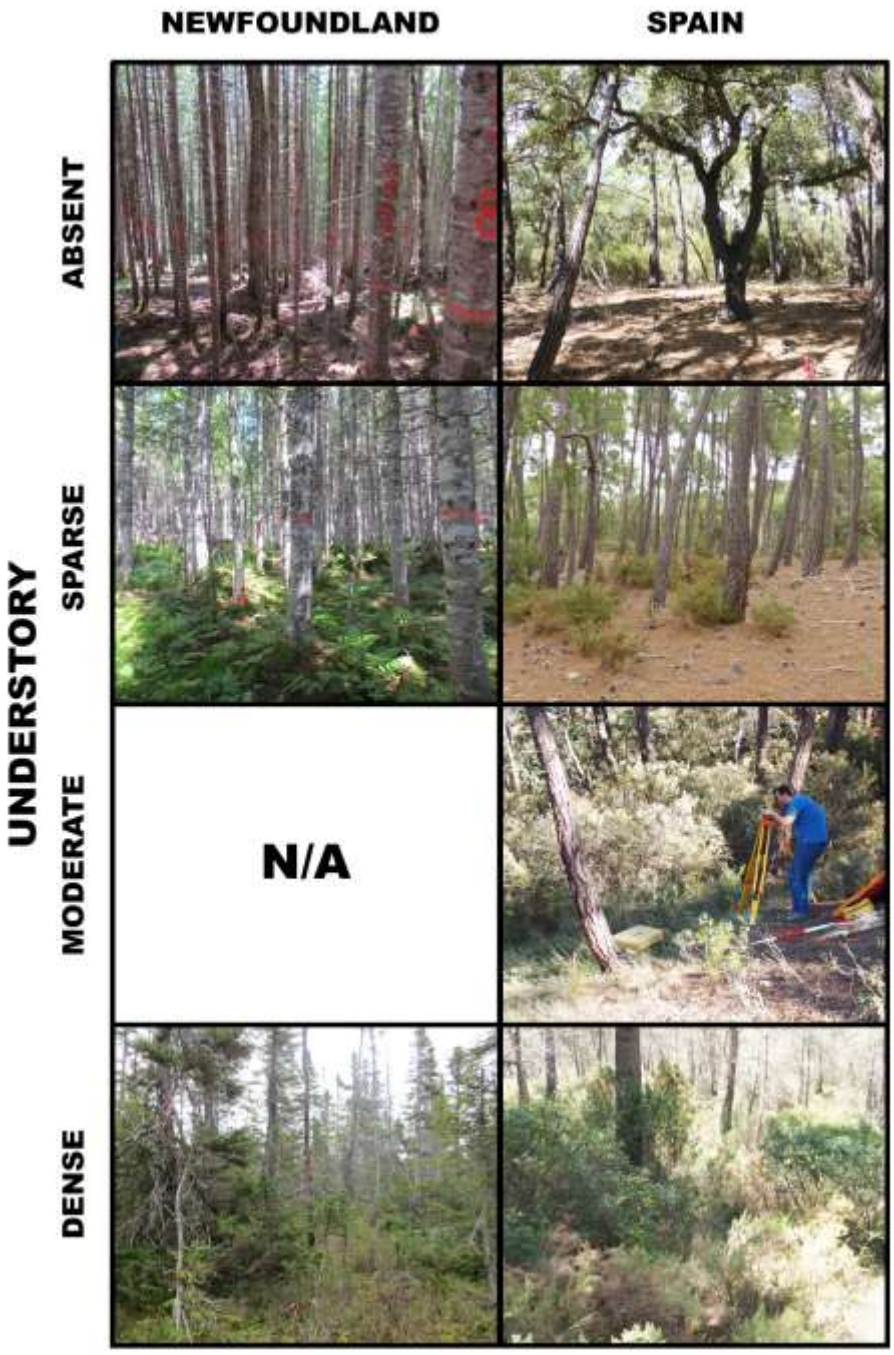

Fig. 2. Field photographs from the Newfoundland and Spain sites illustrating the varying densities of understory vegetation.

2.2. Forest plots

Circular plots were established with a radius of 11.28 m and 15 m for the Newfoundland and Spain sites, respectively. Plot center locations for both sites were measured with a GPS RTK

with an average accuracy of ~0.40 m. Tree species, living status, diameter at breast height, height and canopy base height were measured at all plot locations. For the Newfoundland site, 59 established experimental plots from Luther et al. (2019) were made available with associated ALS_D and ALS_{FW} data, while 70 established experimental plots were made available with similar data for the Spain site (Fig. 1c and d). Among these experimental plots, a structurally representative sample of ten plots was selected per site for TLS sampling by maximizing the variability of canopy cover and understory vegetation for analysis in this study. Regarding canopy cover, we estimated it at plot locations from the proportion of ALS_D first hits to total hits above 2 m per McGaughey (2014). Then, plots with a percentage of first hits above 70% were classified as having a dense canopy cover, between 40% and 70% as having a sparse canopy cover, and below 40%, as having a very sparse canopy cover. Furthermore, we assigned understory vegetation density classes at plot locations through field interpretations and classified plots as having dense, moderate, sparse, or absence of, understory vegetation (Fig. 2). Fig. 3 illustrates the variability in structure from all conifer dominated plots and the structural representativeness of the retained sample plots.

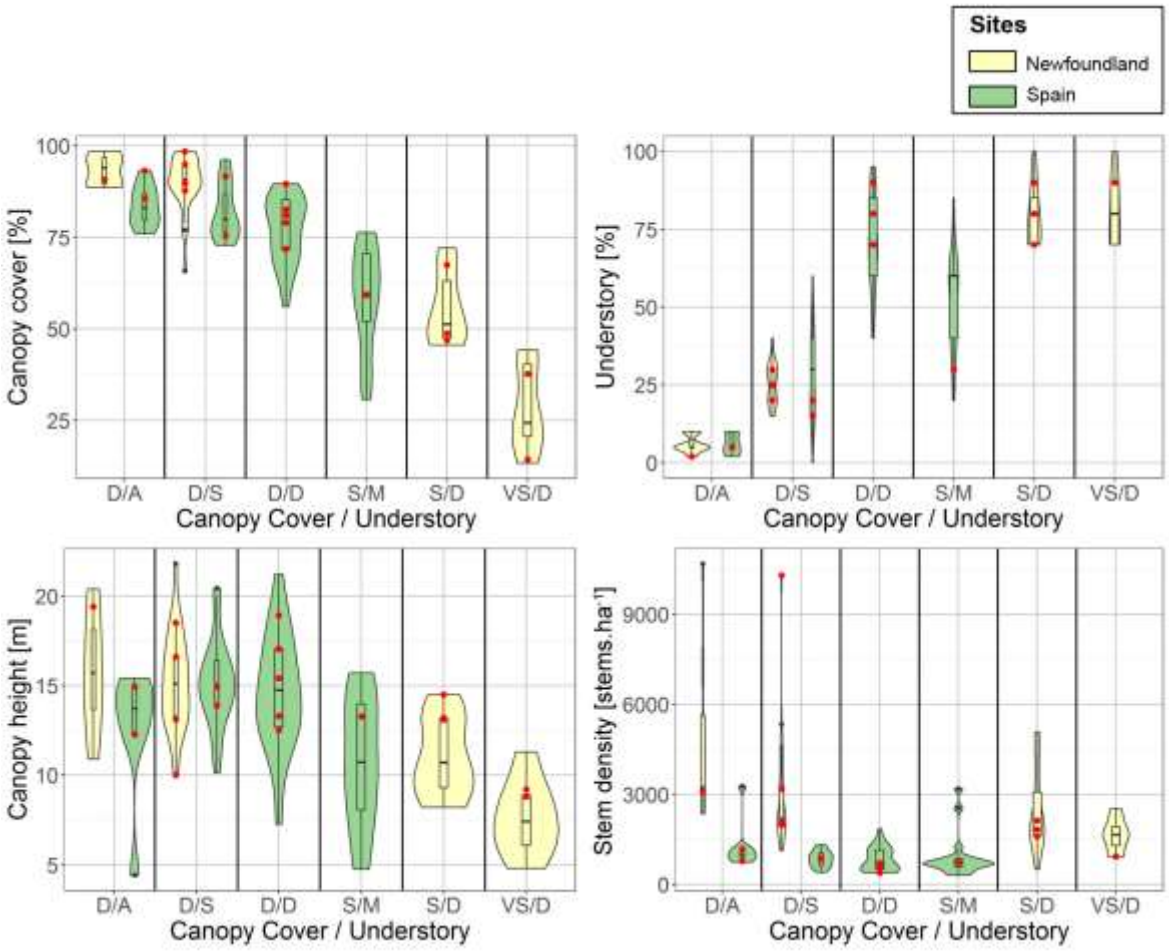

Fig. 3. Violin plots representing four structural attributes (canopy cover, understory, canopy height and stem density) from all available plots. Attribute values for plots retained for analysis are in red. Abbreviations: D-dense; M-moderate; S-sparse; VS-very sparse; A-absent.

2.3. Laser scanning data

In our study, we analyzed laser scanning data obtained from three differing configurations, namely ALS_D, ALS_{FW}, and TLS. The ALS data obtained for the Newfoundland site were acquired between August 15th and September 24th 2016 with a Riegl LMS-Q680i. The approximate flight altitude was 1000 m above ground level. Data were acquired with a pulse frequency of 330 kHz and a scan angle range of ± 30º. Not excluding waterbodies, the overall average laser scanning pulse density was 7.34 pulses·m^{-2}. ALS_{FW} data was discretized by the service provider (Leading Edge Geomatics, Canada) using the Gaussian pulse estimation

computation method to extract ALS_D data. Average point densities of 16 points·m^{-2} were observed at plot locations for ALS_D.

ALS data acquisition at the Spain site was undertaken on September 16th 2015 using an IGI LiteMapper 6800. Flight altitude ranged between 600 and 820 m above ground level. Data were acquired with a pulse frequency of 300 kHz and a scan angle range of ± 30º. The overall average pulse density was 14 pulses·m^{-2}. Again, ALS_{FW} data was discretized by the service provider (IMAO, France) using the Gaussian pulse estimation computation method to extract ALS_D data. Average point densities of 36 points·m^{-2} were observed at plot locations for the Spain site for ALS_D.

The TLS data were collected using a FARO FOCUS 3D 120 phase-based laser scanner using a multi-scan configuration on both sites, recording only the first hit with an angular density between pulses of 0.0036 degree. TLS data for the Newfoundland site were acquired between June and August 2017 while the TLS data for the Spain site were acquired between September 29th and October 23rd, 2015. To minimize signal occlusion, each plot was scanned from nine positions: one at plot center, four at ~15 m from the center in each cardinal direction (i.e., N, W, S, E), and four at ~ 7.5 m and ~ 6 m from the center in each primary intercardinal direction (i.e., NW, SW, SE, NE) for the Spain and Newfoundland sites, respectively. Each scan identified a minimum of three co-registration spherical targets common with adjacent scans. Co-registration of the 9 scans was performed using FARO SCENE software version 6.2 (FARO, Lake Mary, FL). The resulting co-registered point cloud comprised, on average, 392×10^6 hits.

2.4. Overview of the methods

An overview of the methodological approach and associated procedures is presented in Fig. 4. First, ALS_{FW} data were denoised and georeferenced in order to create an ALS_{FW} point cloud compatible with the ALS_D and TLS point clouds (Procedure 1). We then proceeded with the co-registration of the three laser scanning datasets: ALS_{FW}, ALS_D and TLS (Procedure 2). Once co-registered, all the point clouds were represented independently in voxel grids (Procedure 3a). Sampling of each voxel by the laser beams depends primarily on three variables: (*i*) the number of theoretical laser beams passing through the voxel (Nt), (*ii*) the number of these theoretical beams that were occluded prior to reaching the voxel (Nb), and (*iii*), the number of hits returned from these theoretical beams within the voxel (Nh). We then estimated these variables for each voxel of the three datasets (Procedure 3b) in order to derive the vertical distribution profiles from ALS (Nh^{ALS} for both discrete (Nh^{ALSD}) and full waveform (Nh^{ALSFW}) datasets) (Procedure 3c) as well as the Plant Area Density from TLS (PAD^{TLS}) (Procedure 3d), which is the projected surface of the vegetated materials (wood and leaves). In order to quantify and compare signal occlusion within the three laser scanning datasets, we computed for each the rate of pulse reduction of Nt as the proportion of beams blocked prior to reaching the voxel (Nb/Nt) (Procedure 3e). A height normalization was then applied to Nh^{ALS}, PAD^{TLS}, and the rate of pulse reduction from ALS_{FW}, ALS_D and TLS (Procedure 4). This created a coherent vertical leveling between these estimated variables from which we produced vertical profiles of Nh^{ALS}, PAD^{TLS} and the rate of pulse reduction (Procedures 5a and 5b). These vertical profiles were used to analyze the relationship between the detection of vegetative material in different strata from airborne and terrestrial laser scanning configurations and the rate of pulse reduction. We computed the coefficient of correlation at lower strata ($0.5\ m \leq z \leq 4\ m$) to quantify the similarity

of vertical profiles of Nh^{ALSFW} and Nh^{ALSD} with PAD^{TLS}. Afterwards, the lower strata of the Nh^{ALS} vertical profiles were compared to determine which ALS configuration (i.e., ALS_{FW} or ALS_D) depicts the understory vegetation in more detail. An application of the Lorenz curve (Lorenz, 1905) and the Gini index (Gini, 1912) calculated from the Nh^{ALSFW} and Nh^{ALSD} vertical profiles of the lower strata determined the density of understory vegetation, which we compared with field observations. Data processing and analysis was carried out in Python (van Rossum, 1995) and R programming languages (Team, 2013). PAD^{TLS} was computed with the L-Vox algorithm (available in the Computree open source framework (Piboule et al., 2015)).

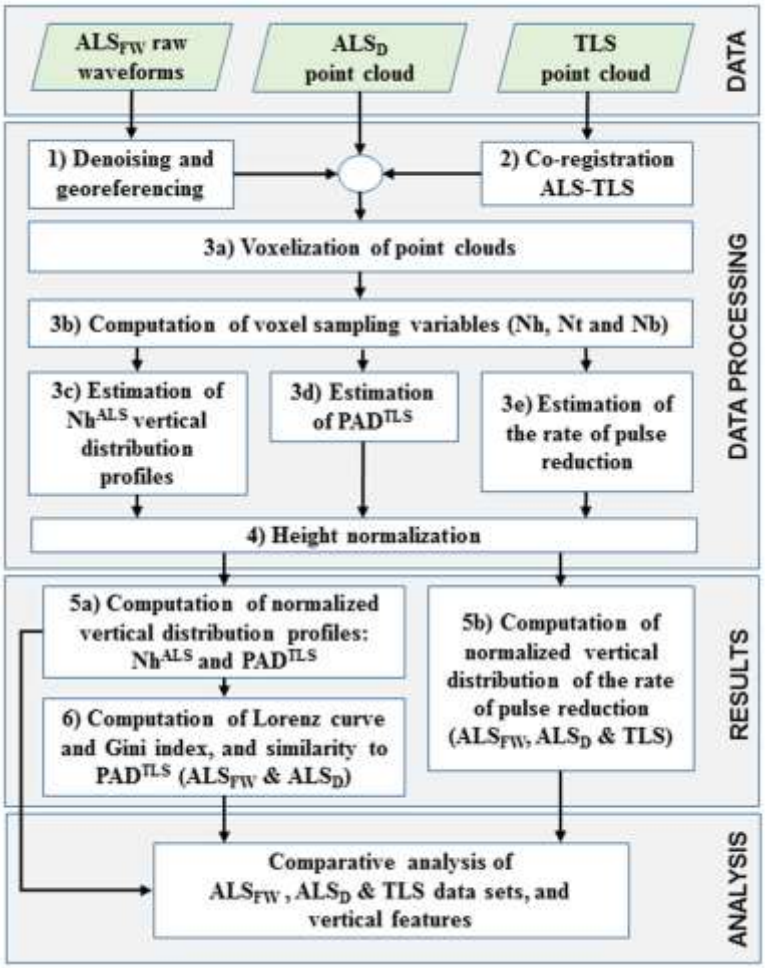

Fig. 4. Overview of the methodological approach. Abbreviations: ALS_{FW}: full-waveform airborne laser scanning, ALS_D: discrete airborne laser scanning, TLS: terrestrial laser scanning, Nh: number of hits, Nt: number of theoretical laser beams, Nb: number of theoretical laser beams

blocked before reaching a given voxel, Nh^{ALS}: number of hits extracted from airborne laser scanning (i.e., full-waveform and discrete), PAD^{TLS}: plant area density extracted from terrestrial laser scanning.

2.5. Data preprocessing

2.5.1. Denoising and georeferencing the waves from ALS_{FW}

Initial data were available in point cloud format for the ALS_D and TLS configurations. Unlike discrete return lidar sensors which record backscattered energy at precisely referenced points in time and space, ALS_{FW} sensors record backscattered energy as a nearly continuous signal in a full-waveform indexed bin. We therefore needed to create an ALS_{FW} point cloud compatible with the ALS_D and TLS point clouds. To do so, we removed the noise contained in the raw ALS_{FW} waveforms and georeferenced the remaining bins (Procedure 1). We adopted the process proposed by Lefsky et al. (2005), and further described by Hermosilla et al. (2014b), which first defines a noise threshold as the mean of the waveform's amplitude summed with four times its standard deviation. All the waveforms whose amplitudes were below this threshold were discarded as noise. After removing noisy waveforms, background noise was suppressed from the remaining waveforms by subtracting a noise value (133% of the mode of the amplitudes) from each amplitude value of the waveform. We then computed each bin's XYZ coordinates from: (*i*) the coordinates of at least one hit belonging to the waveform, (*ii*) the elapsed time between the known hit and the anchor point (i.e., the beginning) of the waveform, (*iii*) the distance between two consecutive bins, and (*iv*) the waveform line parameters Xt, Yt and Zt. The coordinates and orientation of the waveform were derived from the known hit coordinates and waveform line parameters. The coordinates of the anchor point were derived from the known hit coordinates, orientation of the waveform, and elapsed time between the known hit and anchor point. Each bin's XYZ coordinates were then defined by the coordinates of the anchor point, the orientation

of the waveform, and the distance between two consecutive bins. The resulting ALS_{FW} data contained only significant waveforms with the noise removed from which we were able to create a georeferenced point cloud compatible with those from the two other configurations: ALS_D and TLS.

2.5.2. XY co-registration of ALS and TLS datasets

Considering that the main goal of this research is to compare the data obtained from three different laser scanning configurations, it was necessary that all point clouds were co-registered in the same coordinate system (Procedure 2). Co-registration is a critical step to ensure that the three point clouds can be compared in our analysis. Georeferencing of the ALS data followed common practice and was done by registering the flight trajectory coordinates from the airborne GPS to a set of ground control points. These ground control points allowed for an accurate georeferencing of the flight lines, and therefore the resulting waveforms and point clouds. Given that the ALS_D is derived from the ALS_{FW} data, co-registration between these two datasets was not necessary.

Co-registration of the TLS data to the ALS data was performed using the latter as reference. These data were co-registered on a plot-level basis. For each plot, Canopy Height Surfaces (CHS) were generated independently from both ALS_D and TLS data. The geometric distribution of tree crowns and canopy gaps guided the selection of homologous points from both CHS. A 2D affine matrix transformation was then computed from the homologous point coordinates and applied to the TLS point clouds. Only translation in the horizontal plane and rotation around the vertical axis were applied since the distance values from both laser scanner systems needed to be

maintained, therefore not altering the scale. The root-mean-square error (RMSE) of the 2D affine transformation was 9 cm ± 4 cm and 7 cm ± 7 cm for the Newfoundland and Spain data, respectively. The co-registration process was carried out by extracting the coordinates with QGIS open source software (QGIS, 2016) and computing the 2D affine transformation.

2.6. Estimating voxel sampling variables and the rate of pulse reduction

The 3D space of the point clouds was discretized in voxels to produce vertical profiles (Procedure 3a). The point density from the TLS point clouds was sufficiently high to allow the adoption of very small voxels (e.g., ~5cm). However, assessing the capacity of each laser scanning configuration to detect understory vegetation required adopting a common voxel size: a trade-off between the fine vertical features of vegetation density and the availability of sufficient hits from laser scanning signal within a voxel. We therefore adopted a voxel size for all three datasets according to (*i*) the pulse spacing of ALS in XY plane, (*ii*) the temporal sample spacing of ALS_{FW} in the Z axis, and (*iii*), avoiding empty voxels in either datasets (Crespo-Peremarch et al., 2018a). The most suitable voxel size was determined to be 0.5 m in X, 0.5 m in Y and 0.15 m in Z (vertical).

We first computed for all datasets the number of beams crossing the voxel (Nt), the number of hits within the voxel (Nh), and the number of beams blocked prior to reaching the voxel (Nb) (Procedure 3b). The computation approach of these three sampling variables differed between the TLS and ALS datasets due to their distinct sensor-signal-scene configurations. The approach taken for the TLS data used the one (first) hit per pulse of the TLS phase-shift technology. The approach taken for the ALS data assumed that all recorded hits were associated with an

368 independent laser pulse having no cross-section (i.e., a vector with no divergence). This,
369 however, is an abstraction. In fact, multiple hits originate from the same beam. Hence, the
370 sampling variables derived from TLS data are not directly comparable with those derived from
371 ALS data. We therefore assumed the number of hits in each voxel to be a representation of the
372 forest vertical distribution only from ALS for both Nh^{ALSD} and Nh^{ALSFW} (Procedure 3c) while the
373 forest vertical distribution from TLS was represented by the cumulative PAD^{TLS} (Procedure 3d).
374 In addition to Nt, Nh and Nb, the path length of all pulses crossing the voxel was estimated from
375 the TLS data. The three voxel sampling variables and the path length of all pulses crossing the
376 voxel allowed calculating PAD^{TLS}, in $m^2 \cdot m^{-3}$, for each voxel according to the mathematical
377 framework proposed by Pimont et al. (2018). We used a minimum of five pulses reaching a
378 voxel ($Nt\text{-}Nb \geq 5$) as a threshold for calculating PAD^{TLS}, otherwise the voxel was assigned as
379 being occluded. A negligible number of TLS voxels were tagged as occluded due to the large
380 voxel size relative to point density.
381
382 In order to quantify signal occlusion caused by vegetation, we computed the rate of pulse
383 reduction as the proportion of beams blocked prior to reaching the current voxel (Nb/Nt)
384 (Procedure 3e). Knowing the rate of pulse reduction provides insight on the potential or
385 drawbacks of the different laser scanning configurations.
386

387 ## 2.7. Extracting forest vertical distribution and rate of pulse reduction profiles

388 In Section 2.5, through the 2nd procedure, TLS data were co-registered only in XY (not in Z) to
389 the ALS_D data. Absolute heights of the canopy needed to be maintained in order to define the
390 original laser pulse trajectories, which was critical in computing Nh^{ALSD}, Nh^{ALSFW}, PAD^{TLS}, and

391 the rate of pulse reduction. However, in order to extract and make meaningful plot-level
392 comparisons of the vertical profiles of these attributes (stored as 3D matrices of voxels), a co-
393 registration in the Z-axis was necessary (Procedure 4). Co-registration ensured that the base of
394 each column of voxels was set to a common Z reference system where all ground voxels were set
395 to a height of 0 m. Both the ALS and TLS datasets had their respective DTMs created with a cell
396 size of 0.5 m. The DTMs for ALS data were generated from ALS_D data. Classification of ground
397 points was done using the Axelsson algorithm (Axelsson, 2000) implemented in LAStools
398 (Isenburg, 2017). The DTMs for the TLS data were produced for every plot using an open source
399 ground classification algorithm in Computree (Piboule et al., 2015). Height normalization of the
400 3D matrices was therefore done with their respective DTM; e.g., Nh^{ALSD} and Nh^{ALSFW} were
401 normalized to its respective ALS-derived DTM as PAD^{TLS} was normalized to its respective
402 TLS-derived DTM.
403
404 Next, we extracted vertical profiles of these 3D matrices to represent the vertical distribution of
405 forest elements for each horizontal layer of voxels (i.e., a vertical bin with a height of 0.15 m).
406 The value of each vertical bin was calculated as the sum of the voxel values of the corresponding
407 horizontal layer for Nh^{ALSD}, Nh^{ALSFW} and PAD^{TLS} (Procedure 5a). The rate of pulse reduction
408 was calculated as the average of the voxel values for that horizontal layer (Procedure 5b). Only
409 information 0.5 m above the ground was considered therefore removing values associated to an
410 understory zone strongly influenced by soil micro-relief and very low vegetation. This procedure
411 provided the normalized vertical profiles of Nh^{ALSD}, Nh^{ALSFW} and PAD^{TLS}, and the rate of pulse
412 reduction.
413

In order to assess how well we captured the vertical distribution profiles at different heights from ALS, we assessed the relationships between Nh^{ALS} and PAD^{TLS} by means of ratios. To do so, we computed, plotted and compared the ratios between Nh^{ALS} and PAD^{TLS} (i.e., Nh^{ALSD}/PAD^{TLS} and Nh^{ALSFW}/PAD^{TLS}). The resulting vertical profiles highlighted limitations in detecting the different vertical strata based on a unitless indicator. Higher values imply a higher detection of the vegetation, while lower values imply a more limited detection.

2.8. Classifying the vertical distribution of understory vegetation from ALS data

Once the forest vertical profiles were generated for Nh^{ALS}, both ALS configurations (ALS_D and ALS_{FW}) were compared to detect the understory vegetation. The height range for this comparison was set between 0.5 m and 4 m to detect the lower strata through Nh^{ALS} vertical profiles. The upper limit of 4 m was deemed appropriate to capture high shrubs within our study sites. Detection of the understory vegetation was addressed through the characteristics of the Nh^{ALS} vertical profiles, whose curvature depends on the presence of understory vegetation. To quantify the curvature of the Nh^{ALS} vertical profiles, we combined the fitting of the Lorenz curve (Lorenz, 1905) with the Gini index (Gini, 1912) (Procedure 6). The Gini index is a measure of statistical dispersion initially created to measure inequality of countries' wealth. It is computed as the area between the curve and the equality line (i.e., 1:1 line) (see area A in Fig. 5a) divided by the area below the equality line and delimited by the main axes (see area B in Fig. 5a). Fig. 5b and 5c show the two extreme cases, i.e., complete equality (i.e., Gini index = 0) and complete inequality (i.e., Gini index = 1), respectively. Consequently, the Gini index quantifies the curvature of a distribution, or in our application, a vertical profile. The Lorenz curve and Gini index have been widely used in economics, but also in some forestry applications. For instance, Valbuena et al.

(2013) and Valbuena et al. (2014) proposed several indicators describing tree size inequality related to forest vertical structure. These indicators were based on the combined analysis of the Lorenz curve from ALS_D data, including the Gini index. In addition, the Gini index obtained from ALS_D was proposed to identify differences in structural complexity of forests (Valbuena et al., 2016).

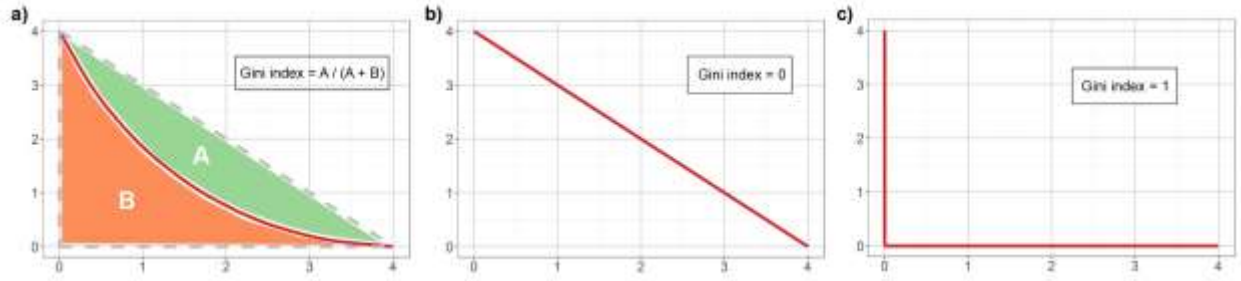

Fig. 5. Description of the Gini index for (a) a general case, and two examples showing (b) equality (i.e., Gini index = 0) and (c) inequality cases (i.e., Gini index = 1), respectively.

In our study, each Nh^{ALS} vertical profile (Nh^{ALSD} and Nh^{ALSFW}) is represented by a Lorenz curve. The Gini index was estimated from this Lorenz curve through the ratio A / (A + B) (Fig. 5a, 6b). To do so, we applied the following three steps:

1. Nh^{ALS} vertical profiles were first filtered to exclude overstory following the same procedure for ALS_{FW} and ALS_D. We discarded the Nh^{ALS} values in the vertical profiles that had a height greater than the first relative minimum of Nh^{ALS} (see Fig. 6b). Consequently, high shrubs were included in the analysis but lower crowns were excluded from the computation of the Gini index (see Fig. 6a).

2. Nh^{ALS} values were then normalized between 0 and 1 using Eq. (1) (see Fig. 6c). The normalization facilitated the comparison between plots since Nh^{ALS} values are variable according to the different plots and acquisition configurations.

$$Nh^{ALS}{}_{norm} = \frac{Nh^{ALS} - min\ (Nh^{ALS})}{max\ (Nh^{ALS}) - min\ (Nh^{ALS})} \quad (1)$$

where $Nh^{ALS}{}_{norm}$ refers to the normalization (between 0 and 1) of Nh^{ALS}. Also, $min(Nh^{ALS})$ and $max(Nh^{ALS})$ are the minimum and maximum values, respectively, of Nh^{ALS} for the current plot between 0.5 and 4 m.

3. Finally, the Gini index was computed as the area between the curve and the equality line divided by the area below the equality line and delimited by the main axes (see Fig. 6c). Application of the Gini index was performed using the *ineq* package (Zeileis et al., 2009) in the R programming language (Team, 2013).

The PAD estimation of the lower strata from the TLS data is a far less affected by signal occlusion because of the position of the scanner. Therefore the PAD^{TLS} vertical profile was used as a reference to compare the ability of ALS_{FW} and ALS_D to detect understory vegetation. Nh^{ALS} vertical profiles were compared with PAD^{TLS} by calculating the correlation coefficient at lower strata ($0.5\ m \leq z \leq 4\ m$) and its significance using the Student's t-test (Gosset, 1908). This coefficient is a unitless quantity, and therefore allows comparing different datasets with different units and orders of magnitude, such as Nh^{ALSFW}, Nh^{ALSD} and PAD^{TLS} vertical profiles.

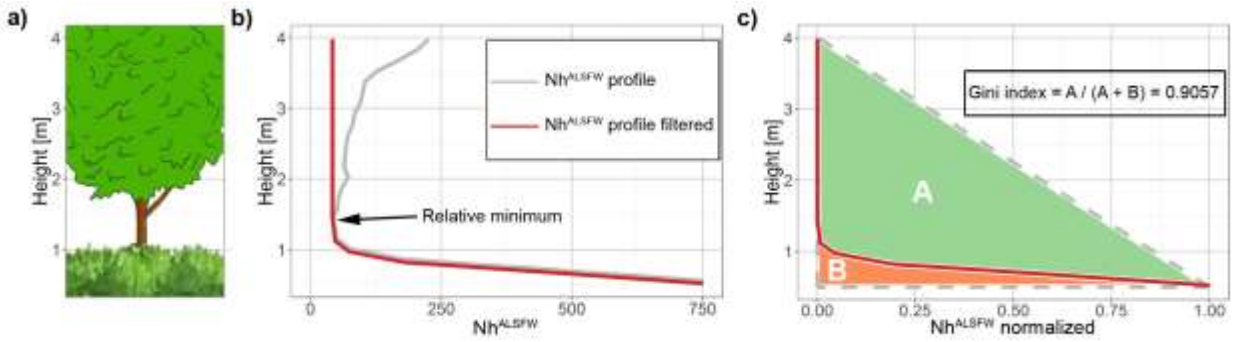

Fig. 6. Depiction of (a) separation between understory vegetation and overstory, (b) the filtering of Nh^{ALSFW} vertical profile corresponding to the lower strata from plot P3-NF and Nh^{ALSFW} vertical profile, and (b) estimation of the Gini index from the resulting Nh^{ALS} vertical profile.

3. Results

3.1. Forest vertical distribution and rate of pulse reduction profiles

The data processing steps led to a representation of the vertical distribution and rate of pulse reduction profiles from the three laser scanning configurations, shown for a sample of plots from the Newfoundland and Spain sites in Fig. 7 and 8, respectively. Overall, results show that ALS, viewing the forest from the top-down, was more limited to sample the lower strata, while TLS, viewing the forest from bottom-up, was more limited to sample the top of the canopy. Despite these limitations, the vertical distribution profiles generally represented the forest's vertical structure, capturing components of the different vertical strata. For instance, plot P5-SP (Fig. 8b) has a mixed presence of maritime pines and cork oaks. This heterogeneous vertical structure was represented by different peaks in associated PAD^{TLS} vertical profiles. Conversely, plots with a homogeneous vertical structure (e.g., plot P7-SP, Fig. 8c) were represented by a single and well-defined peak in their associated vertical distribution profiles. A visual comparison between vertical distribution profiles (i.e., PAD^{TLS}, Nh^{ALSD} and Nh^{ALSFW}) and associated rated of pulse reduction with the one meter wide point cloud transects reveals an obvious correlation: both

vertical profiles of element distribution and point cloud density decreased as the rate of pulse reduction increased. The rate of pulse reduction profiles generally followed a distribution in the form of a sigmoid function or "S"-shaped curve, whose form, or increment of slope of the rate of pulse reduction, depended on the laser scanning configuration as well as the density of the upper canopy. For example, all plots with dense canopy cover (e.g., Fig. 7a, 7b, 8a, 8b, and 8d) had rate of pulse reduction profiles following a clearly defined sigmoid distribution. However, converse trends were observed in the rate of pulse reduction from ALS and TLS: increasing rates of pulse reduction were associated with decreasing heights from ALS and increasing heights from TLS. Furthermore, in some instances, observed high values in the rate of pulse reduction were associated with very low values from the vertical distribution profiles (i.e., where PAD^{TLS} and/or Nh^{ALS} reached or approached 0). This occurred more frequently for Newfoundland plots where conifer species on this site grow dense, creating a dense upper canopy (e.g., P2-NF and P4-NF in Fig. 7a and 7b, respectively). For these plots, the rate of pulse reduction profiles transition to high values (i.e., 35-40% for TLS; 80-90% for ALS) at heights of ~10-13 m. Conversely, for plots with sparsely distributed vegetation, the rate of pulse reduction was very low. In conditions of sparse vegetation, the rate of pulse reduction curve followed the typical sigmoid distribution, however did not reach the high values observed from denser plots (e.g., P7-SP in Fig. 8c). Sparse and very sparse sites often displayed a relatively flat vertical line, terminating near the ground by a steep high value (e.g., P6-NF and P10-NF in Fig. 7c and 7d). Overall, but more specifically in dense canopy covers, an offset in the x-values from the midstory strata of PAD^{TLS} was observed relative to Nh^{ALS}. This offset coincides with the large discrepancy in the number of hits returned by ALS and TLS systems from the midstory strata, where ALS did not detect tree stems to the same degree as TLS. On the other hand, little variability was observed in Nh^{ALSD} vertical profiles

in the lower strata, except in some cases where canopy cover was very sparse (e.g., P10-NF). The analysis of vertical distribution profiles from the lower strata generally showed lower Nh^{ALSD} when compared to Nh^{ALSFW}. In addition, similarity in overall shape, quantified and reported in section 3.2 by means of the coefficient of correlation, was greater between Nh^{ALSFW} and PAD^{TLS} than between Nh^{ALSD} and PAD^{TLS}. Furthermore, Nh^{ALSFW} values had an exponential increment as they approached the ground when understory vegetation was absent. This trend was less obvious in plot P4-NF and most Newfoundland plots with higher rates of pulse reduction (> 80%).

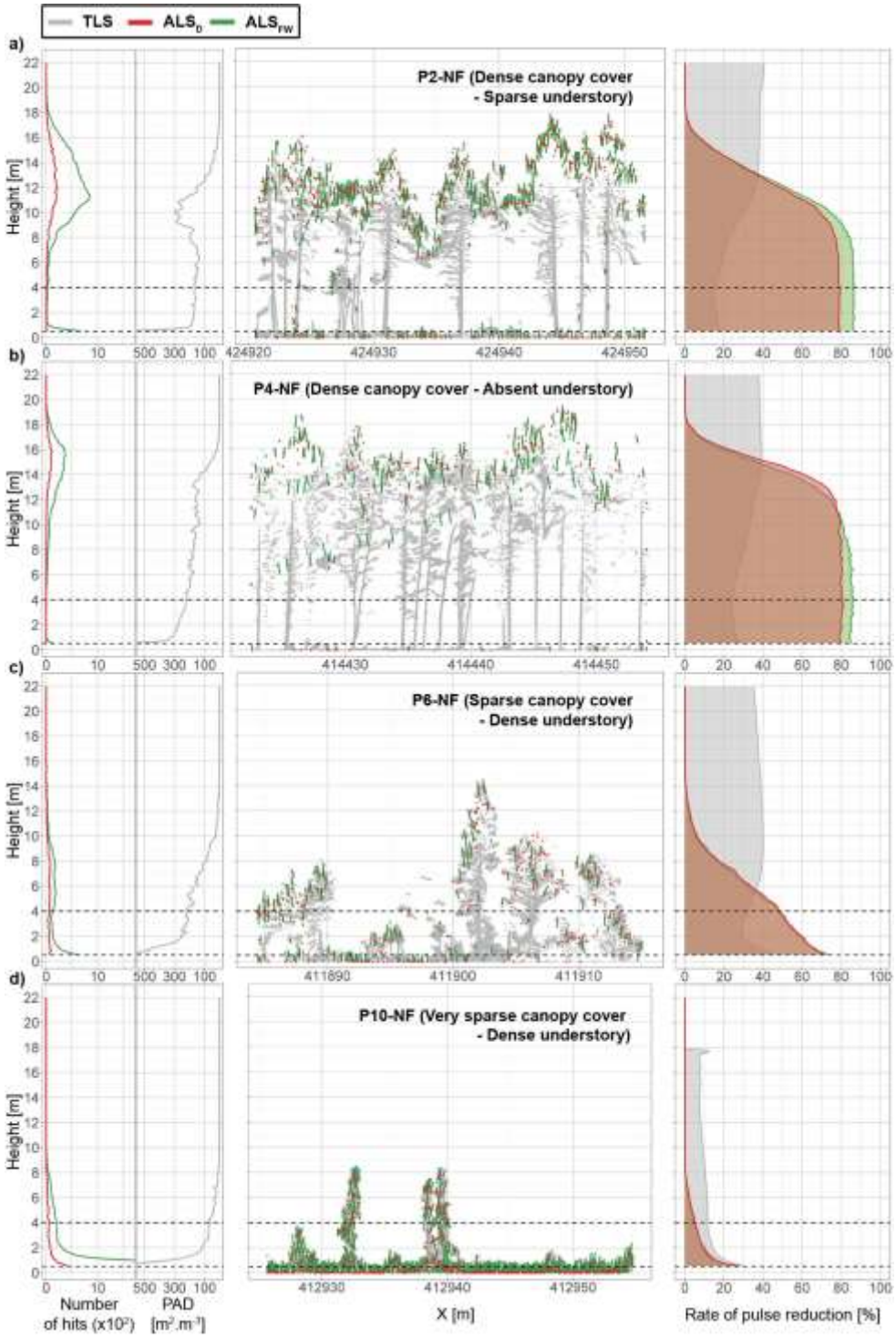

Fig. 7. Vertical profiles representing four plots of the Newfoundland site (a-d). The three figures from left to right represent: (i) the number of hits from ALS and cumulative Plant Area Density from TLS, (ii) a point cloud transect of one meter wide, and (iii) the rate of pulse reduction from the three configurations (i.e., TLS, ALS_D and ALS_{FW}). Dashed lines represent the limits of the lower strata (i.e., 0.5 and 4 m).

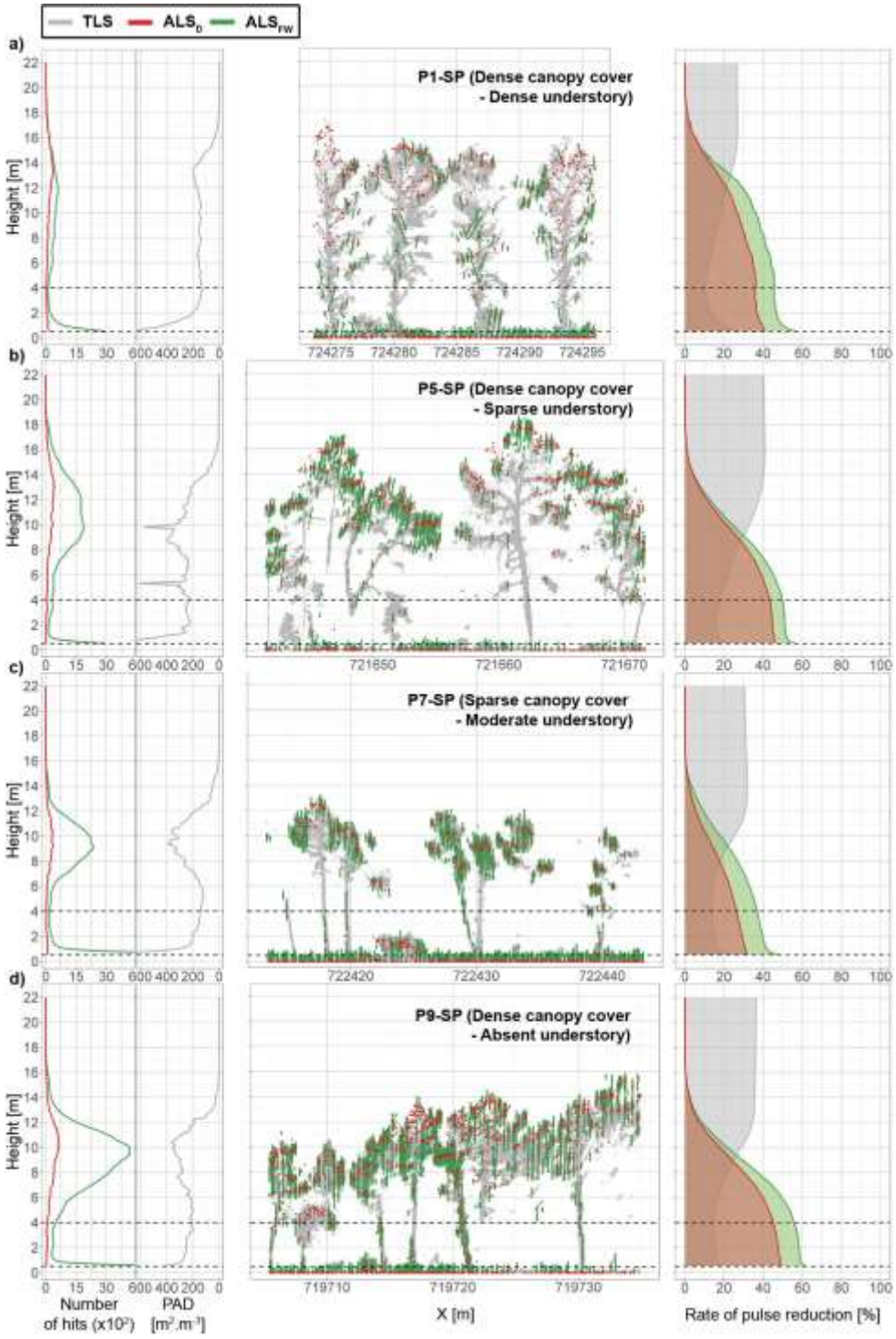

Fig. 8. Vertical profiles representing four plots of the Spain site (a-d). The figures from left to right represent: (i) the number of hits from ALS and cumulative Plant Area Density from TLS, (ii) a point cloud transect of one meter wide, and (iii) the rate of pulse reduction from the three configurations (i.e., TLS, ALS_D and ALS_{FW}). Dashed lines represent the limits of the lower strata (i.e., 0.5 and 4 m).

Considering TLS as reference, the ratios between Nh^{ALS} and PAD^{TLS} in Fig. 9 illustrate the limitations of ALS configurations in detecting the vertical distribution profiles at different heights based on a unitless indicator. Ratios were calculated as Nh^{ALS} divided by PAD^{TLS}, therefore implying higher detection of vegetation as this ratio value increases. The highest values for the ratio calculated from Nh^{ALSD} were observed in the upper strata for all plots (Fig. 9). In most cases, ALS_D incoming pulses were blocked by the dominant strata, generating signal occlusion underneath. ALS_{FW} (Nh^{ALSFW}/PAD^{TLS}) and ALS_D (Nh^{ALSD}/PAD^{TLS}) ratio values were most similar in the upper strata. Nevertheless, ALS_{FW} ratio values below the dominant strata (i.e., intermediate and/or lower strata) remained high, while ALS_D ratio values dropped. Generally, ALS_D ratios dropped below 1 m, and in some cases below 2.5 m (e.g., P10-NF in Fig. 9).

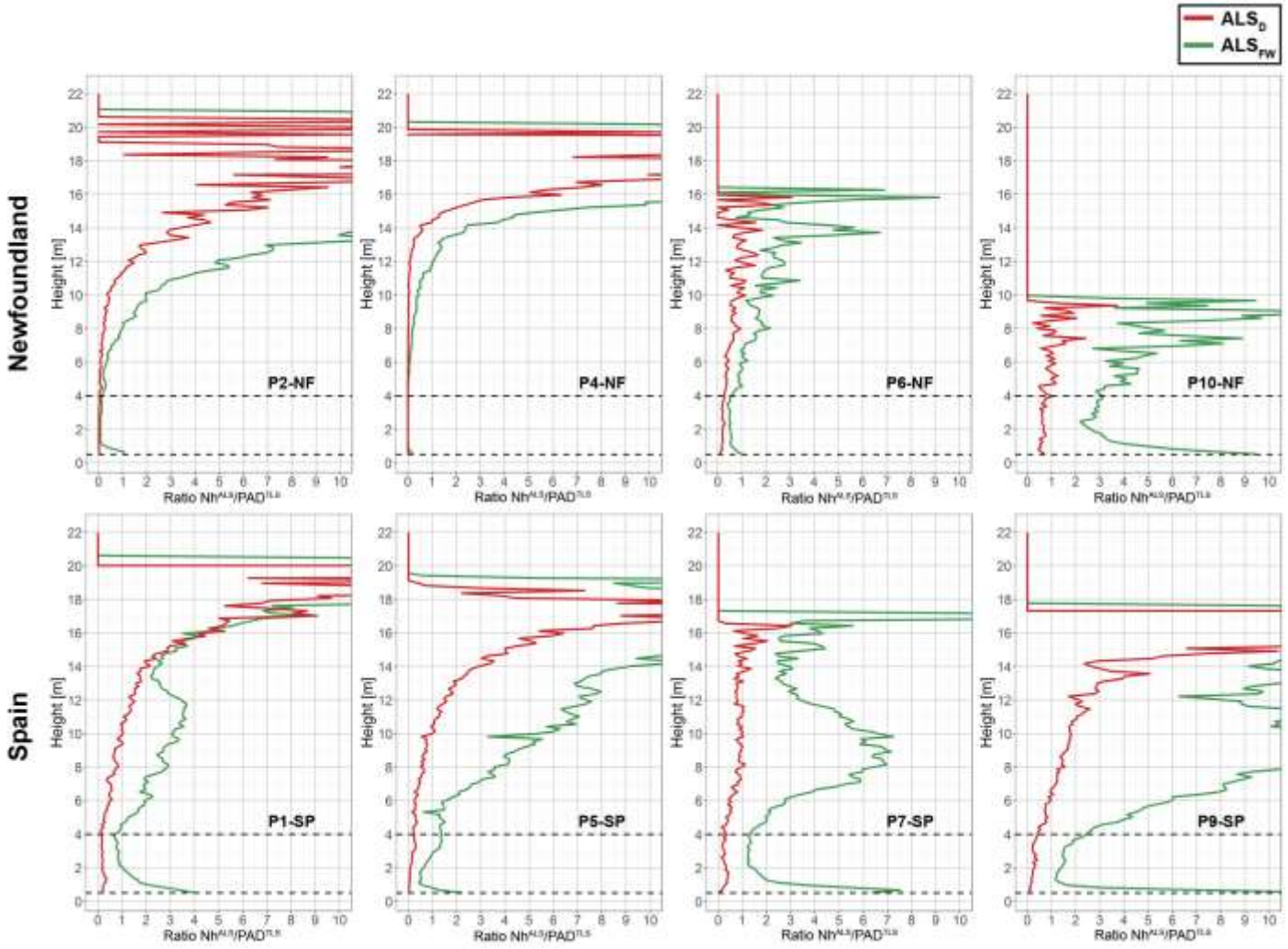

Fig. 9. Vertical profiles representing the ratio (Nh^{ALS}/PAD^{TLS}) between the Nh from ALS (i.e., ALS_{FW} in green and ALS_D in red) and cumulative PAD from TLS for a sample of plots. Dashed lines represent the limits of the lower strata (i.e., 0.5 and 4 m).

3.2. Understory characterization from ALS

In the previous subsection it was observed that although the values of the vertical distribution profiles may differ between Nh^{ALS} and PAD^{TLS}, they remained similar in terms of shape, albeit with different units and order of magnitude. This similarity in terms of shape of the vertical distribution profiles was quantified between Nh^{ALS} and PAD^{TLS} by using the coefficient of correlation (see Table 1), which ultimately allows for determining whether understory vegetative material was detected. Coefficients of correlation were calculated between Nh^{ALS} (i.e., Nh^{ALSFW} and Nh^{ALSD}) and PAD^{TLS} vertical profiles from the lower strata. Null coefficient of correlation values (e.g., observed from ALS_D for plots P4-NF, P5-NF and P6-SP, and for plot P6-SP from ALS_{FW}) were due to the fact that no values were registered at the lower strata, and therefore the standard deviations of the corresponding vertical profiles were equal to zero. Coefficients of correlation between Nh^{ALSFW} and PAD^{TLS} were rarely below 90%, and all were considered to be significant correlations according to the Student's t-test (Table 1). The range of coefficients of correlation for ALS_{FW} was between 53.48% and 99.58%, with an average value of 90.11% and an associated standard error of 3.04%. On the other hand, with the exception of plot P9-NF, all coefficients of correlation between Nh^{ALSD} and PAD^{TLS} were all lower or at par, with one correlation not being considered as significant (plot P7-SP). The range of coefficients of correlation for ALS_D was between 30.60% and 97.36%, with an average value of 82.57% and an associated standard error of 4.29%. Regarding summary statistics of the differences in coefficients of correlation between ALS_{FW} and ALS_D, the range was between 22.01% and -68.36% (being negative values when coefficients of correlation for ALS_{FW} were greater), with an average value of -9.50% and an associated standard error of 4.62%. Hence, although ALS_{FW} detected understory vegetation with a much larger number of hits than ALS_D (see Figures 7, 8

584 and 9), the latter still had a significant correlation with PAD^{TLS}. Remarkably, strong correlations
585 between Nh^{ALSFW} and PAD^{TLS} were observed for dense canopy cover plots from the
586 Newfoundland site, where the rate of pulse reduction was large in lower strata. For instance,
587 plots P2-NF and P4-NF had rates of pulse reduction ~85% for ALS_{FW} at the lower strata and an
588 associated coefficient of correlation with PAD^{TLS} equal to 98.50% and 93.39%, respectively.
589 Nh^{ALSFW} and Nh^{ALSD} were equally correlated with PAD^{TLS} (i.e., < 1% of difference) in only a
590 few plots having a dense canopy cover (plots P8-SP and P10-SP) and in a plot with very sparse
591 canopy cover (plot P10-NF).

592

593 **Table 1.** Coefficient of correlation values between Nh^{ALS} (i.e., Nh^{ALSFW} and Nh^{ALSD}) and
594 PAD^{TLS} as reference at the lower strata.
595

Site	Plot ID	Correlation Nh^{ALSFW}-PAD^{TLS} (%)	Correlation Nh^{ALSD}-PAD^{TLS} (%)
Newfoundland	P1-NF	63.25	56.21
	P2-NF	98.50	97.36
	P3-NF	92.95	88.09
	P4-NF	93.39	NA
	P5-NF	NA	NA
	P6-NF	95.66	67.40
	P7-NF	98.09	87.29
	P8-NF	96.06	90.46
	P9-NF	69.77	91.78
	P10-NF	96.64	96.70
Spain	P1-SP	96.89	92.31
	P2-SP	98.73	67.89
	P3-SP	99.58	91.13
	P4-SP	98.78	96.97
	P5-SP	94.96	84.02
	P6-SP	53.48	NA
	P7-SP	98.96	30.60*
	P8-SP	89.89	90.46
	P9-SP	84.37	82.16
	P10-SP	92.21	92.93

596 * Correlation deemed not significant from Student's t-test with a confidence level of 95%.

597

3.3. Understory vegetation density classification

Afterwards, the variation of the Nh^{ALS} vertical profiles at the lower strata was quantified by means of the Gini index, whose values for ALS_D and ALS_{FW} are presented in Table 2. Generally, sparse understory vegetation densities had large Gini indices (i.e., gradual increments of Nh^{ALS}), while dense understory vegetation had low Gini indices (i.e., steep increments of Nh^{ALS}). Despite considerable differences between the structure of Boreal and Mediterranean forests, the Gini index values confirmed a coherent behaviour for both sites as a vegetation density indicator. Specific Gini index ranges derived from the Nh^{ALSFW} vertical profiles were associated to understory vegetation density classes as follows: absent (91.63% ± 0.13), sparse (90.59% ± 2.23), moderate (84.31% ± 0.00), and dense (75.45% ± 7.86). Similarly, from the Nh^{ALSD} vertical profiles, Gini index ranges were associated to understory vegetation density classes as follows: absent (97.69% ± 4.01), sparse (83.79% ± 12.31), moderate (53.38% ± 0.00) and dense (59.37% ± 16.71). Nevertheless, the Gini index class interval thresholds computed from ALS_D were fuzzier, implying more overlap between classes, than those from ALS_{FW}. Class intervals derived from computed Gini index values showed larger standard deviations for ALS_D than ALS_{FW}. Furthermore, misclassification between sparse and absent understory vegetation density classes occurred when derived with ALS_D data. Some plots with a moderate or sparse understory had a Gini index from Nh^{ALSD} lower than plots with a dense understory vegetation (e.g., P7-SP vs. P3-SP), which lead to a misclassification. Similarly, plot P5-NF, with sparse understory vegetation, had a Gini index from Nh^{ALSFW} larger than that observed for plots with absent understory, which also lead to a misclassification.

620 **Table 2.** Gini index from Nh^{ALSFW} and Nh^{ALSD} vertical profiles for each plot from the
621 Newfoundland and Spain sites. Plots are in ascending order according to the Gini index
622 computed from Nh^{ALSFW}.
623

Plot ID	Understory vegetation	Canopy cover	Gini index Nh^{ALSFW} (%)	Gini index Nh^{ALSD} (%)
P9-NF	Dense	Very Sparse	59.63	33.47
P6-NF	Dense	Sparse	65.10	45.97
P1-SP	Dense	Dense	72.65	55.04
P2-SP	Dense	Sparse	74.98	51.21
P7-NF	Dense	Sparse	75.74	89.94
P4-SP	Dense	Dense	78.88	60.13
P10-NF	Dense	Very sparse	80.09	66.87
P10-SP	Dense	Dense	80.12	69.82
P8-NF	Dense	Sparse	83.03	45.25
P3-SP	Dense	Dense	84.27	76.04
P7-SP	Moderate	Sparse	84.31	53.38
P8-SP	Sparse	Dense	86.83	64.14
P2-NF	Sparse	Dense	90.55	79.33
P3-NF	Sparse	Dense	90.57	90.71
P5-SP	Sparse	Dense	90.61	77.81
P1-NF	Sparse	Dense	91.14	94.91
P4-NF	Absent	Dense	91.48	100.00
P9-SP	Absent	Dense	91.67	93.06
P6-SP	Absent	Dense	91.74	100.00
P5-NF	Sparse	Dense	93.81	95.83

624

625 # 4. Discussion

626 In this study, we assessed the ability of different laser scanning configurations to estimate
627 vertical forest structure, linking it with a new method to estimate signal occlusion in the different
628 strata. In addition, we also assessed and compared the suitability of ALS_{FW} and ALS_D to classify
629 in understory vegetation density classes. Key results highlighted the limitations inherent to
630 different configurations in estimating vertical forest structure and the importance of signal
631 occlusion. More specifically, in the lower strata, which is highly occluded by ALS
632 configurations, understory vegetation density was successfully assessed through vertical canopy

density profiles. Moreover, the analysis of vertical profiles from our testing plots demonstrated that ALS_{FW} improved understory identification and density estimation over ALS_{D}.

Overall, our results confirmed the general trend largely accepted by the scientific community, which implies that laser scanning signal occlusion prevails in sectors blocked by dense canopy covers. Signal occlusion therefore depends largely on the laser scanning configuration: ALS, viewing the forest from the top-down, is more limited to sample the lower strata, while TLS, viewing the forest from bottom-up, is more limited to sample the top of the canopy (Hilker et al., 2012; Anderson et al., 2016; Crespo-Peremarch and Ruiz, 2017). Regarding ALS configurations, canopy density of the upper layer is the single most important environmental factor in defining if sufficient airborne laser pulses reach the complete vertical range of the forest. Hence, signal occlusion can limit exhaustive sampling of the lower vertical strata with ALS data. In this sense, Maltamo et al. (2014) distinguished between signal occlusion and canopy cover as two different but related phenomena, both affecting the overestimation of canopy base height when using ALS. Conversely, for plots with sparsely distributed vegetation, the level of signal occlusion is very low. Consequently, estimation of the distribution of vegetative material is possible throughout the vertical range of the forest. In these cases, vertical distribution of forest materials can be estimated with high level of accuracy. LaRue et al. (2020) also observed that estimating canopy density of the lower strata is best achieved in open canopy covers for ALS configurations, because of the influence of signal occlusion caused by dense canopy covers.

In cases where significant signal occlusion exists, ALS configurations detection of lower strata density capabilities are limited. The reliability of vertical distribution profiles is directly

dependent on the level of signal occlusion. In this regard, we proposed to use the rate of pulse reduction as an indicator of the amount of signal occlusion occurring at various heights in the forest. Inferring the ability to detect vertical distribution from our reference dataset (PAD^{TLS}) and the plotted values of rate of pulse reduction profiles led us to propose a threshold of the rate of pulse reduction from which the estimation of the distribution of vegetative material is no longer possible. This threshold is variable and related to the density of the canopy cover, which remains plot-specific. We noticed that Nh^{ALS} values between the height with a rate of pulse reduction above ~80-90% and the ground do not provide reliable estimates of vegetation density. A similar principle, reversed vertically, applies to TLS datasets where PAD^{TLS} between the height with a rate of pulse reduction above ~35-40% and the top of the canopy. The slope of the rate of pulse reduction curve, which follows a sigmoid function, depends on the laser scanning configuration as well as the density of the upper canopy. Currently we suggest an approximate threshold for the rate of pulse reduction. The ability to define a more specific threshold may be tied to parameters of this sigma curve as a discriminating indicator of the overall signal occlusion and defining the vertical area where vegetation density can be estimated.

ALS_{FW} and ALS_D data come from the same signal, however, further processing steps before obtaining the final product make them different. Using the complete (i.e., ALS_{FW}) or the discretized (i.e., ALS_D) signal in the detection of the top of the canopy is not significantly different to assess vegetation density. Nonetheless, ALS_{FW} provided a definite advantage to detect vegetation density for intermediate and lower strata than ALS_D. Lower strata are generally occluded due to overstory blocking incoming laser pulses. Consequently, Nh^{ALSD} vertical profiles do not show much features in the lower strata, except in some cases where signal

679 occlusion caused by overstory is low (e.g., very sparse canopy cover). Nevertheless, when using
680 PAD^{TLS} as reference, Nh^{ALS} (i.e., Nh^{ALSFW} and Nh^{ALSD}) vertical profiles correlations are
681 considered as significant, albeit Nh^{ALSFW} is more correlated. Although curve correlation is more
682 accurate, and the number of hits much larger at the lower strata with ALS_{FW}, our results
683 confirmed that understory vegetation was captured by ALS_D, albeit to a lesser extent and in plots
684 with a high rate of pulse reduction (i.e., ~85%). Other studies have also found difficulties
685 associated with ALS_D to detect the internal forest structure (Chasmer et al., 2006; Hilker et al.,
686 2010; Hilker et al., 2012). The higher potential of ALS_{FW} when compared with ALS_D to detect
687 and determine understory vegetation density classes was also found in several studies (Hancock
688 et al., 2017; Crespo-Peremarch et al., 2018b; Torralba et al., 2018). Our results confirm the
689 potential of both ALS configurations to detect non-occluded strata (i.e., top of the canopy) and
690 demonstrated the increased capability of ALS_{FW} to detect strata with signal occlusion (i.e.,
691 intermediate and lower strata). Although ALS_D may be used to estimate understory vegetation at
692 a plot-level, the signal is generally weak in dense canopies and hence limits the estimation of
693 density in the lower strata at such fine spatial scales.
694
695 Vertical profiles with Nh^{ALSFW} display a systematic artefact near the ground in the form of an
696 exponential increment, even if understory vegetation is absent. This increment depends mainly
697 on two factors: the large number of hits from the ground and the hits from the understory
698 vegetation. The histogram of hits from the ground usually follows a Gaussian curve for which
699 the upper side can be merged by the hit from understory, if present. When understory is present,
700 generally variation of the Nh^{ALSFW} values relates to the understory vegetation density classes,
701 whereas Nh^{ALSD} values are not responsive, except for open canopies with a rate of pulse

reduction below ~50%. Regardless, the number of hits from the ground dominates to the point of masking the understory signal in most situations. Hence, although Nh^{ALSFW} vertical profiles increase exponentially as they approach the ground for all the understory vegetation scenarios, variation of Nh^{ALSFW} increment can be used to identify and determine understory vegetation density classes.

We demonstrated the Gini index to be a useful and accurate indicator to determine understory vegetation density classes from either Nh^{ALS} vertical profiles. Our results demonstrated that understory vegetation density classes can be identified and further grouped by processing the ALS data in both dense and porous forests. Despite strong signal at lower heights in the forest, ALS and especially ALS_{FW}, the Gini index identifies understory densities. Additionally, Gini index thresholds established for understory vegetation densities coincide for both sites: Boreal and Mediterranean. Thus, the understory vegetation density classes are represented by the following Gini value ranges from Nh^{ALSFW}: below a value of ~85% for dense understory vegetation density, between ~85% and ~90% for sparse, and above ~90% for absent. Fortunately, and contrary to ALS_D, misclassification from ALS_{FW} is not occurring between sparse and other understory vegetation density classes. In a related study, Valbuena et al. (2012) discriminated forest structural types by using an application of the Lorenz curve and the Gini index based on the basal area and the number of trees. Apart from a Gini index of 0% and 100% representing the complete equality and inequality, respectively, they also found that a value of 50% was relevant. This value represents a uniform distribution of the basal area of the trees. However, with our datasets, Gini index values from Nh^{ALSFW} were all above 56%, since the Lorenz curves start increasing below the height considered as upper limit of the lower strata (i.e.,

4 m), and therefore Gini index values are higher. Other indicators such as L-Skewness (Valbuena et al., 2017) and Shannon Index (Almeida et al., 2019) are complementary to Gini index. L-skewness allows for quantifying the asymmetry of the Lorenz curve. This facilitates estimating mean height and absence of understory vegetation. Additionally, the Shannon Index represents the diversity of the dataset using a variable as reference (e.g., species). Therefore, it would be feasible to use height thresholds as a variable to determine understory vegetation density classes. Nonetheless, when signal occlusion caused by overstory is important, the ability to use the Shannon or Gini indices is strongly compromised. It is therefore critical to estimate the level of signal occlusion by means of the rate of pulse reduction prior to carry out the analysis.

We proposed a simple way to identify the understory vegetation layer and exclude the overstory. The procedures most frequently adopted in the literature apply a threshold at 2 m height assuming that it covers the understory vegetation. This procedure is non-discriminant, not plot-specific, and therefore it may exclude shrubs or include lower crowns. Instead, we propose considering the vertical distribution of gaps in the density profiles to identify a local minimum separating overstory from understory vegetation. This results in different height values delimiting understory vegetation from overstory, which for our dataset varied between 0.525 and 3.975 m. The accuracy of this procedure depends on vegetation homogeneity. This vertical gap assessment was done at a plot-level, but it can also be applied at a finer scale (e.g., at voxel-column) if a minimum hit density is reached for all heights to avoid false gaps. The procedure we proposed is plot-specific and allows for an automatic height division of overstory and understory vegetation layers.

Some limitations in the application of the developed methodological procedure are noteworthy. Currently, PAD estimates are limited to being derived from TLS data, as the estimation of PAD from ALS configurations is currently not possible. The unbiased estimation of PAD from the mathematical framework proposed by Pimont et al. (2018) decreases significantly the influence of signal occlusion for a reliable representation of vertical profiles. Therefore, it is a useful reference to represent distribution of vertical structure. PAD estimation from all the configurations would have allowed for a comparison in the detection of the vertical distribution profiles. Unfortunately, no methods were currently available to estimate PAD from multiple returns ALS data. Nevertheless, the number of hits in the ALS data in the non occluded areas can be used as a unitless indicator (i.e., coefficient of correlation) comparable with PAD^{TLS}. Furthermore, we note that the Gini index was successful in determining understory vegetation density classes from both airborne and terrestrial laser scanning data, but can not be implemented with emerging full-waveform spaceborne laser scanning data such as GEDI (Global Ecosystem Dynamics Investigation) (Dubayah et al., 2020). GEDI emits four laser beams with a large footprint (~19-25 m) that do not overlap. The method proposed in this study assumes that many laser beams cross a same voxel, and then the number of hits is used as a driving variable to calculate the Gini index. Nevertheless, other metrics based on return amplitude (Crespo-Peremarch and Ruiz, 2020) may be more suited to characterize understory vegetation on large areas with GEDI.

Knowing the limitations of laser scanning configurations is fundamental to use lidar point clouds for the estimation of forest canopy structure. The most severe limitation is caused by signal occlusion by vegetative elements, which can be quantified with the rate of pulse reduction.

771 Despite high level of signal occlusion in the lower strata for ALS configurations, the proposed
772 method allows estimating presence and density of understory vegetation in both dense and
773 porous canopies of Boreal and Mediterranean forests through the Gini index applied to ALS_{FW}
774 data. This new indicator becomes one of the few options to characterize understory vegetation
775 for ALS configurations, which has many implications for forest ecology and wildfire mitigation.
776

777 # 5. Conclusions

778 This study assessed the limitations and potentials of airborne and terrestrial laser scanning
779 configurations to estimate the vertical forest structure. We conclude that understory vegetation
780 density classes can successfully be determined more accurately with ALS_{FW} than with ALS_D.
781 More specifically, three key points stand out from our study. Firstly, the rate of pulse reduction
782 profiles was demonstrated to be a good indicator to quantify signal occlusion along the vertical
783 profile. This information can be used to determine the reliability of vegetation density estimates
784 from different laser scanning configurations for specific vertical strata. Secondly, both ALS
785 configurations (discrete and full waveform) showed their capability to detect understory
786 vegetation, albeit significantly more accurately with ALS_{FW} due to the greater number of hits
787 registered in lower strata. The considerably lower number of hits registered from ALS_D in the
788 lower strata suggests that a forest plot would be the finest spatial scale (i.e. minimal mapping
789 unit) for which understory vegetation can be successfully detected, and hence, our methods could
790 be applied to. Finer scales would inevitably lack sufficient registered hits in understory
791 vegetation for accurate understory characterization. Finally, and thirdly, we demonstrated the use
792 of the Gini index as a way to determine understory vegetation density classes from both ALS
793 configurations, again, more accurately with ALS_{FW}. Understory vegetation density classes

(absent, sparse, moderate and dense) were defined through thresholds applied to the index for both ALS_{FW} and ALS_{D}. Computing the rate of pulse reduction and Gini index characterized the vertical structure and understory vegetation of these structurally differing forests. The applications for which this contribution may be relevant are several, such as characterizing wildlife habitats, assessing timber productivity and improving silvicultural decision-making in support of wildfire mitigation. Further research is needed to better understand the relationships between estimates of PAD and vertical profiles of number of hits for ALS configurations, vertical profiles of rate of pulse reduction and classification of forest types, and the use of the Gini indicator to estimate presence and density of understory vegetation.

6. Acknowledgments

This research was mainly developed in the Centre d'Applications et de Recherche en TÉLédétection of Université de Sherbrooke, Canada. The authors are thankful for the financial support provided by the Spanish Ministerio de Economía y Competitividad and FEDER, in the framework of the project CGL2016-80705-R, and also the Canadian research project Assessment of Wood Attributes using Remote Sensing (AWARE) (NSERC CRDPJ-462973-14, grantee N.C. Coops, UBC).

7. References

Almeida, D.R.A., Stark, S.C., Chazdon, R., Nelson, B.W., Cesar, R.G., Meli, P., Gorgens, E.B., Duarte, M.M., Valbuena, R., Moreno, V.S., Mendes, A.F., Amazonas, N., Gonçalves, N.B., Silva, C.A., Schietti, J., Brancalion, P.H.S., 2019. The effectiveness of lidar remote sensing

816 for monitoring forest cover attributes and landscape restoration. For. Ecol. Manage. 438,
817 34-43. https://doi.org/10.1016/j.foreco.2019.02.002
818 Anderson, K., Hancock, S., Disney, M., Gaston, K.J., 2016. Is waveform worth it? A comparison
819 of LiDAR approaches for vegetation and landscape characterization. Remote Sens. Ecol.
820 Conserv. 2, 5–15. https://doi.org/10.1002/rse2.8
821 Axelsson, P., 2000. DEM generation from laser scanner data using adaptive TIN models. Int.
822 Arch. Photogramm. Remote Sens. 33, 111–118.
823 Béland, M., Widlowski, J.-L., Fournier, R.A., 2014. A model for deriving voxel-level tree leaf
824 area density estimates from ground-based LiDAR. Environ. Model. Softw. 51, 184–189.
825 https://doi.org/10.1016/j.envsoft.2013.09.034
826 Bottalico, F., Chirici, G., Giannini, R., Mele, S., Mura, M., Puxeddu, M., McRoberts, R.E.,
827 Valbuena, R., Travaglini, D., 2017. Modeling Mediterranean forest structure using airborne
828 laser scanning data. Int. J. Appl. Earth Obs. Geoinf. 57, 145–153.
829 https://doi.org/10.1016/j.jag.2016.12.013
830 Cao, L., Coops, N., Hermosilla, T., Dai, J., 2014a. Estimation of forest structural variables using
831 small-footprint full-waveform LiDAR in a subtropical forest, China. 3rd Int. Work. Earth
832 Obs. Remote Sens. Appl. EORSA 2014 - Proc. 443–447.
833 https://doi.org/10.1109/EORSA.2014.6927930
834 Cao, L., Coops, N.C., Hermosilla, T., Innes, J., Dai, J., She, G., 2014b. Using small-footprint
835 discrete and full-waveform airborne LiDAR metrics to estimate total biomass and biomass
836 components in subtropical forests. Remote Sens. 6, 7110–7135.
837 https://doi.org/10.3390/rs6087110
838 Cao, L., Coops, N.C., Innes, J.L., Dai, J., Ruan, H., She, G., 2016. Tree species classification in

839 subtropical forests using small-footprint full-waveform LiDAR data. Int. J. Appl. Earth Obs.
840 Geoinf. 49, 39–51. https://doi.org/10.1016/j.jag.2016.01.007
841 Chasmer, L., Hopkinson, C., Treitz, P., 2006. Investigating laser pulse penetration through a
842 conifer canopy by integrating airborne and terrestrial lidar. Can. J. Remote Sens. 32, 116–
843 125. https://doi.org/10.5589/m06-011
844 Chen, Y., Zhu, X., Yebra, M., Harris, S., Tapper, N., 2016. Strata-based forest fuel classification
845 for wild fire hazard assessment using terrestrial LiDAR. J. Appl. Remote Sens. 10, 046025.
846 https://doi.org/10.1117/1.JRS.10.046025
847 Crespo-Peremarch, P., Ruiz, L.Á., Balaguer-Beser, Á., 2016. A comparative study of regression
848 methods to predict forest structure and canopy fuel variables from LiDAR full-waveform
849 data. Rev. Teledetec. 27–40. https://doi.org/10.4995/raet.2016.4066
850 Crespo-Peremarch, P., Ruiz, L.Á., 2017. Análisis comparativo del potencial del ALS y TLS en la
851 caracterización estructural de la masa forestal basado en voxelización. Actas XVII Congr. la
852 Asoc. Española Teledetección. Nuevas plataformas y sensores teledetección 131–135.
853 Crespo-Peremarch, P., Ruiz, L.Á., Balaguer-Beser, Á., Estornell, J., 2018a. Analyzing the role of
854 pulse density and voxelization parameters on full-waveform LiDAR-derived metrics. ISPRS
855 J. Photogramm. Remote Sens. 146, 453–464. https://doi.org/10.1016/j.isprsjprs.2018.10.012
856 Crespo-Peremarch, P., Tompalski, P., Coops, N.C., Ruiz, L.Á., 2018b. Characterizing understory
857 vegetation in Mediterranean forests using full-waveform airborne laser scanning data.
858 Remote Sens. Environ. 217, 400–413. https://doi.org/10.1016/j.rse.2018.08.033
859 Crespo-Peremarch, P., Ruiz, L.A., 2020. A full-waveform airborne laser scanning metric
860 extraction tool for forest structure modelling. Do scan angle and radiometric correction
861 matter? Remote Sens. 12, 292. https://doi.org/10.3390/rs12020292

Dubayah, R., Blair, J.B., Goetz, S., Fatoyinbo, L., Hansen, M., Healey, S., Hofton, M., Hurtt, G., Kellner, J., Luthcke, S., Armston, J., Tang, H., Duncanson, L., Hancock, S., Jantz, P., Marselis, S., Patterson, P.L., Qi, W., Silva, C., 2020. The Global Ecosystem Dynamics Investigation: High-resolution laser ranging of the Earth's forests and topography. Sci. Remote Sens. 1, 100002. https://doi.org/10.1016/j.srs.2020.100002

Giannetti, F., Puletti, N., Quatrini, V., Travaglini, D., Bottalico, F., Corona, P., Chirici, G., 2018. Integrating terrestrial and airborne laser scanning for the assessment of single-tree attributes in Mediterranean forest stands. Eur. J. Remote Sens. 51, 795–807. https://doi.org/10.1080/22797254.2018.1482733

Gini, C., 1912. Variabilità e mutabilità.

González-Ferreiro, E., Diéguez-Aranda, U., Miranda, D., 2012. Estimation of stand variables in Pinus radiata D. Don plantations using different LiDAR pulse densities. Forestry 85, 281–292. https://doi.org/10.1093/forestry/cps002

Gosset, W.S., 1908. The Probable Error of a Mean. Biometrika 6, 1–25. https://doi.org/10.2307/2331554

Greaves, H.E., Vierling, L.A., Eitel, J.U.H., Boelman, N.T., Magney, T.S., Prager, C.M., Griffin, K.L., 2015. Estimating aboveground biomass and leaf area of low-stature Arctic shrubs with terrestrial LiDAR. Remote Sens. Environ. 164, 26–35. https://doi.org/10.1016/j.rse.2015.02.023

Hancock, S., Anderson, K., Disney, M., Gaston, K.J., 2017. Measurement of fine-spatial-resolution 3D vegetation structure with airborne waveform lidar: Calibration and validation with voxelised terrestrial lidar. Remote Sens. Environ. 188, 37–50. https://doi.org/10.1016/j.rse.2016.10.041

885 Heinzel, J., Koch, B., 2011. Exploring full-waveform LiDAR parameters for tree species
886 classification. Int. J. Appl. Earth Obs. Geoinf. 13, 152–160.
887 https://doi.org/10.1016/j.jag.2010.09.010
888 Hermosilla, T., Ruiz, L.A., Kazakova, A.N., Coops, N.C., Moskal, L.M., 2014a. Estimation of
889 forest structure and canopy fuel parameters from small-footprint full-waveform LiDAR
890 data. Int. J. Wildl. Fire 23, 224–233. https://doi.org/10.1071/WF13086
891 Hermosilla, T., Coops, N.C., Ruiz, L.A., Moskal, L.M., 2014b. Deriving pseudo-vertical
892 waveforms from small-footprint full-waveform LiDAR data. Remote Sens. Lett. 5, 332–
893 341. https://doi.org/10.1080/2150704X.2014.903350
894 Hevia, A., Álvarez-González, J.G., Ruiz-Fernández, E., Prendes, C., Ruiz-González, A.D.,
895 Majada, J., González-Ferreiro, E., 2016. Modelling canopy fuel and forest stand variables
896 and characterizing the influence of thinning in the stand structure using airborne LiDAR.
897 Rev. Teledetección 41–55. https://doi.org/10.4995/raet.2016.3979
898 Hilker, T., van Leeuwen, M., Coops, N.C., Wulder, M.A., Newnham, G.J., Jupp, D.L.B.,
899 Culvenor, D.S., 2010. Comparing canopy metrics derived from terrestrial and airborne laser
900 scanning in a Douglas-fir dominated forest stand. Trees 24, 819–832.
901 https://doi.org/10.1007/s00468-010-0452-7
902 Hilker, T., Coops, N.C., Newnham, G.J., van Leeuwen, M., Wulder, M.A., Stewart, J., Culvenor,
903 D.S., 2012. Comparison of terrestrial and airborne LiDAR in describing stand structure of a
904 thinned lodgepole pine forest. J. For. 110, 97–104. https://doi.org/10.5849/jof.11-003
905 Hill, R.A., Broughton, R.K., 2009. Mapping the understorey of deciduous woodland from leaf-
906 on and leaf-off airborne LiDAR data: A case study in lowland Britain. ISPRS J.
907 Photogramm. Remote Sens. 64, 223–233. https://doi.org/10.1016/j.isprsjprs.2008.12.004

Isenburg, M., 2017. LAStools.

Jung, S.-E., Kwak, D.-A., Park, T., Lee, W.-K., Yoo, S., 2011. Estimating crown variables of individual trees using airborne and terrestrial laser scanners. Remote Sens. 3, 2346–2363. https://doi.org/10.3390/rs3112346

Kankare, V., Vastaranta, M., Holopainen, M., Räty, M., Yu, X., Hyyppä, J., Hyyppä, H., Alho, P., Viitala, R., 2013a. Retrieval of forest aboveground biomass and stem volume with airborne scanning LiDAR. Remote Sens. 5, 2257–2274. https://doi.org/10.3390/rs5052257

Kükenbrink, D., Schneider, F.D., Leiterer, R., Schaepman, M.E., Morsdorf, F., 2017. Quantification of hidden canopy volume of airborne laser scanning data using a voxel traversal algorithm. Remote Sens. Environ. 194, 424–436. https://doi.org/10.1016/j.rse.2016.10.023

LaRue, E.A., Wagner, F.W., Fei, S., Atkins, J.W., Fahey, R.T., Gough, C.M., Hardiman, B.S., 2020. Compatibility of aerial and terrestrial LiDAR for quantifying forest structural diversity. Remote Sens. 12, 1407. https://doi.org/10.3390/rs12091407

Lefsky, M.A., Harding, D.J., Keller, M., Cohen, W.B., Carabajal, C.C., Del Bom Espirito-Santo, F., Hunter, M.O., de Oliveira Jr., R., 2005. Estimates of forest canopy height and aboveground biomass using ICESat. Geophys. Res. Lett. 32. https://doi.org/10.1029/2005GL023971

Liang, X., Kankare, V., Hyyppä, J., Wang, Y., Kukko, A., Haggrén, H., Yu, X., Kaartinen, H., Jaakkola, A., Guan, F., Holopainen, M., Vastaranta, M., 2016. Terrestrial laser scanning in forest inventories. ISPRS J. Photogramm. Remote Sens. 115, 63–77. https://doi.org/10.1016/j.isprsjprs.2016.01.006

Lin, Y., Herold, M., 2016. Tree species classification based on explicit tree structure feature

parameters derived from static terrestrial laser scanning data. Agric. For. Meteorol. 216, 105–114. https://doi.org/10.1016/j.agrformet.2015.10.008

Lindberg, E., Olofsson, K., Holmgren, J., Olsson, H., 2012. Estimation of 3D vegetation structure from waveform and discrete return airborne laser scanning data. Remote Sens. Environ. 118, 151–161. https://doi.org/10.1016/j.rse.2011.11.015

Liu, L., Pang, Y., Li, Z., Si, L., Liao, S., 2017. Combining airborne and terrestrial laser scanning technologies to measure forest understorey volume. Forests 8, 111. https://doi.org/10.3390/f8040111

Lorenz, M.O., 1905. Methods of measuring the concentration of wealth. Publ. Am. Stat. Assoc. 9, 209–219.

Luther, J.E., Fournier, R.A., van Lier, O.R., Bujold, M., 2019. Extending ALS-based mapping of forest attributes with medium resolution satellite and environmental data. Remote Sens. 11, 1092. https://doi.org/10.3390/rs11091092

Maltamo, M., Næsset, E., Vauhkonen, J., 2014. Foresty applications of airborne laser scanning. Springer, Netherlands (2014).

Martin-Ducup, O., Schneider, R., Fournier, R.A., 2016. Response of sugar maple (Acer saccharum, Marsh.) tree crown structure to competition in pure versus mixed stands. For. Ecol. Manage. 374, 20–32. https://doi.org/10.1016/j.foreco.2016.04.047

Martin-Ducup, O., Schneider, R., Fournier, R.A., 2017. A method to quantify canopy changes using multi-temporal terrestrial lidar data: Tree response to surrounding gaps. Agric. For. Meteorol. 237–238, 184–195. https://doi.org/10.1016/j.agrformet.2017.02.016

Martinuzzi, S., Vierling, L.A., Gould, W.A., Falkowski, M.J., Evans, J.S., Hudak, A.T., Vierling, K.T., 2009. Mapping snags and understory shrubs for a LiDAR-based assessment of

wildlife habitat suitability. Remote Sens. Environ. 113, 2533–2546. https://doi.org/10.1016/j.rse.2009.07.002

McGaughey, R.J., 2014. FUSION/LDV: Software for LiDAR data analysis and visualization, Manual.

Morsdorf, F., Mårell, A., Koetz, B., Cassagne, N., Pimont, F., Rigolot, E., Allgöwer, B., 2010. Discrimination of vegetation strata in a multi-layered Mediterranean forest ecosystem using height and intensity information derived from airborne laser scanning. Remote Sens. Environ. 114, 1403–1415. https://doi.org/10.1016/j.rse.2010.01.023

Nie, S., Wang, C., Zeng, H., Xi, X., Li, G., 2017. Above-ground biomass estimation using airborne discrete-return and full-waveform LiDAR data in a coniferous forest. Ecol. Indic. 78, 221–228. https://doi.org/10.1016/j.ecolind.2017.02.045

Olsoy, P.J., Glenn, N.F., Clark, P.E., Derryberry, D.R., 2014. Aboveground total and green biomass of dryland shrub derived from terrestrial laser scanning. ISPRS J. Photogramm. Remote Sens. 88, 166–173. https://doi.org/10.1016/j.isprsjprs.2013.12.006

Piboule, A., Krebs, M., Esclatine, L., Hervé, J.-C., 2015. Computree: A collaborative platform for use of terrestrial lidar in dendrometry, in: International IUFRO Conference MeMoWood. Nancy, France.

Pimont, F., Allard, D., Soma, M., Dupuy, J.-L., 2018. Estimators and confidence intervals for plant area density at voxel scale with T-LiDAR. Remote Sens. Environ. 215, 343–370. https://doi.org/10.1016/j.rse.2018.06.024

QGIS, D.T., 2016. QGIS Geographic Information System.

Ravaglia, J., Fournier, R.A., Bac, A., Véga, C., Côté, J.-F., Piboule, A., Rémillard, U., 2019. Comparison of three algorithms to estimate tree stem diameter from terrestrial laser scanner

977 data. Forests 10, 599. https://doi.org/10.3390/f10070599
978 Ruiz, L.A., Hermosilla, T., Mauro, F., Godino, M., 2014. Analysis of the influence of plot size
979 and LiDAR density on forest structure attribute estimates. Forests 5, 936–951.
980 https://doi.org/10.3390/f5050936
981 Ruiz, L.Á., Recio, J.A., Crespo-Peremarch, P., Sapena, M., 2018. An object-based approach for
982 mapping forest structural types based on low-density LiDAR and multispectral imagery.
983 Geocarto Int. 33, 443–457. https://doi.org/10.1080/10106049.2016.1265595
984 Srinivasan, S., Popescu, S., Eriksson, M., Sheridan, R., Ku, N.-W., 2015. Terrestrial laser
985 scanning as an effective tool to retrieve tree level height, crown width, and stem diameter.
986 Remote Sens. 7, 1877–1896. https://doi.org/10.3390/rs70201877
987 Team, R.C., 2013. R: A language and environment for statistical computing.
988 Torralba, J., Crespo-Peremarch, P., Ruiz, L.Á., 2018. Assessing the use of discrete, full-
989 waveform LiDAR and TLS to classify Mediterranean forest species composition. Rev.
990 Teledetección 27–40. https://doi.org/10.4995/raet.2018.11106
991 Treitz, P., Lim, K., Woods, M., Pitt, D., Nesbitt, D., Etheridge, D., 2012. LiDAR sampling
992 density for forest resource inventories in Ontario, Canada. Remote Sens. 4, 830–848.
993 https://doi.org/10.3390/rs4040830
994 Valbuena, R., Packalen, P., Marti, S., Maltamo, D., 2012. Diversity and equitability ordering
995 profiles applied to study forest structure. For. Ecol. Manage. 276, 185-195.
996 https://doi.org/10.1016/j.foreco.2012.03.036
997 Valbuena, R., Packalen, P., Mehtätalo, L., García-Abril, A., Maltamo, M., 2013. Characterizing
998 forest structural types and shelterwood dynamics from Lorenz-based indicators predicted by
999 airborne laser scanning. Can. J. For. Res. 43, 1063–1074. https://doi.org/10.1139/cjfr-2013-

0147

Valbuena, R., Vauhkonen, J., Packalen, P., Pitkänen, J., Maltamo, M., 2014. Comparison of airborne laser scanning methods for estimating forest structure indicators based on Lorenz curves. ISPRS J. Photogramm. Remote Sens. 95, 23–33. https://doi.org/10.1016/j.isprsjprs.2014.06.002

Valbuena, R., Eerikäinen, K., Packalen, P., Maltamo, M., 2016. Gini coefficient predictions from airborne lidar remote sensing display the effect of management intensity on forest structure. Ecol. Indic. 60, 574–585. https://doi.org/10.1016/j.ecolind.2015.08.001

Valbuena, R., Maltamo, M., Mehtätalo, L., Packalen, P., 2017. Key structural features of Boreal forests may be detected directly using L-moments from airborne lidar data. Remote Sens. Environ. 194, 437–446. https://doi.org/10.1016/j.rse.2016.10.024

van Rossum, G., 1995. Python tutorial, technical report CS-R9526. Amsterdam, The Netherlands.

Vaughn, N.R., Moskal, L.M., Turnblom, E.C., 2012. Tree species detection accuracies using discrete point lidar and airborne waveform lidar. Remote Sens. 4, 377–403. https://doi.org/10.3390/rs4020377

Vierling, L.A., Xu, Y., Eitel, J.U.H., Oldow, J.S., 2013. Shrub characterization using terrestrial laser scanning and implications for airborne LiDAR assessment. Can. J. Remote Sens. 38, 709–722. https://doi.org/10.5589/m12-057

Watt, P.J., Donoghue, D.N.M., 2005. Measuring forest structure with terrestrial laser scanning. Int. J. Remote Sens. 26, 1437–1446. https://doi.org/10.1080/01431160512331337961

Wing, B.M., Ritchie, M.W., Boston, K., Cohen, W.B., Gitelman, A., Olsen, M.J., 2012. Prediction of understory vegetation cover with airborne lidar in an interior ponderosa pine

1023 forest. Remote Sens. Environ. 124, 730–741. https://doi.org/10.1016/j.rse.2012.06.024

1024 Zeileis, A., Kleiber, C., Zeileis, M.A., 2009. Package “ineq.”

1025